UNIVERSIDAD DE CHILE
FACULTAD DE CIENCIAS FÍSICAS Y MATEMÁTICAS
DEPARTAMENTO DE INGENIERÍA ELÉCTRICA

EXPERIMENTAL STUDY OF THE ASTROMETRIC CRAMÉR-RAO LIMIT ON BIDIMENSIONAL DIGITAL DETECTORS

MEMORIA PARA OPTAR AL TÍTULO DE INGENIERA CIVIL ELÉCTRICA

CLAUDIA ISABEL JESÚS SAN MARTÍN LUQUE

PROFESOR GUÍA:
RENÉ ALEJANDRO MÉNDEZ BUSSARD

MIEMBROS DE LA COMISIÓN:
MARIO GAI
ANDRÉS CABA

SANTIAGO DE CHILE
2021

RESUMEN DE LA MEMORIA PARA OPTAR
AL TÍTULO DE INGENIERA CIVIL ELÉCTRICA
POR: **CLAUDIA ISABEL JESÚS SAN MARTÍN LUQUE**
FECHA: 2021
PROF. GUÍA: RENÉ ALEJANDRO MÉNDEZ BUSSARD

EXPERIMENTAL STUDY OF THE ASTROMETRIC CRAMÉR-RAO LIMIT ON BIDIMENSIONAL DIGITAL DETECTORS

La medición de la posición de los astros es un tema fundamental en múltiples áreas de la astronomía, especialmente en la astrometría, cuyo desarrollo depende de la obtención de mejores imágenes con mayor calidad utilizando una mayor cantidad de detectores y más avanzados. En este contexto es crucial el estudio de la máxima precisión alcanzable en la determinación de la posición utilizando un detector digital bidimensional, en particular, un CCD o un CMOS, debido a la posible aparición de limitaciones como por ejemplo, la interferencia entre pixeles o el ruido espacial.

Con el objetivo de investigar este tema, fue diseñado e implementado un montaje experimental simple, enfocado en el estudio de la máxima precisión alcanzable de manera experimental al medir la posición de una estrella y su posterior comparación con el límite astrométrico de Cramér-Rao teórico, que corresponde a la máxima precisión alcanzable en la determinación de la posición. Utilizando este montaje y análisis de datos, se estimó la desviación estándar experimental de la posición de las estrellas por medio de múltiples tipos de algoritmos de centrado de imágenes.

Los resultados obtenidos fueron utilizados como retroalimentación para la mejora del montaje experimental, logrando obtener un set de datos que cumplía las condiciones necesarias para el estudio. Finalmente, los datos lograron alcanzar una precisión del orden de $\frac{1}{200}$ de pixel, lo que corresponde a aproximadamente 0.0284μm, con una gran calidad de imagen y fuentes puntuales bien muestreadas, asegurando el correcto comportamiento de los algoritmos de centrado utilizados.

Estos resultados finales fueron comparados con el límite de Cramér-Rao astrométrico, lo que permitió la verificación experimental del comportamiento de límite de la cota de Cramér-Rao. Además, se analizó el comportamiento de cada algoritmo de centrado de imágenes aplicado, junto con un mayor dominio y comprensión de los aspectos relevantes de la configuración experimental.

RESUMEN DE LA MEMORIA PARA OPTAR
AL TÍTULO DE INGENIERA CIVIL ELÉCTRICA
POR: **CLAUDIA ISABEL JESÚS SAN MARTÍN LUQUE**
FECHA: 2021
PROF. GUÍA: RENÉ ALEJANDRO MÉNDEZ BUSSARD

EXPERIMENTAL STUDY OF THE ASTROMETRIC CRAMÉR-RAO LIMIT ON BIDIMENSIONAL DIGITAL DETECTORS

The measurement of the position of celestial objects is a fundamental issue for several branches of astronomy, specially for astrometry, which development depends on the obtaining of better images with higher quality using more and better detectors. For this purpose, it is crucial to study the best location accuracy achievable with a bidimensional digital detector, for example, a CCD or a CMOS, due to the possible appearance of limitations as pixel crosstalk or spatial noise.

In order to investigate this subject, a simple experimental setup was implemented, aimed at the study of the higher precision achievable experimentally measuring the position of a star, and its comparison with the theoretical Cramér-Rao astrometric limit, which corresponds to the maximum achievable location accuracy. Using this setup and data analysis, the experimental standard deviation of the position of the stars was estimated using several types of image centering algorithms.

This results were used as feedback to improve the experimental setup, reaching a data set that satisfied the necessary conditions for the study. Finally, the obtained data reached accuracy values of the order of $\frac{1}{200}$ of a pixel, which corresponds to approximately 0.0284μm, with great image quality and well sampled point-like sources, ensuring the good behavior of the applied location algorithms.

This final results were compared with the astrometric Cramér-Rao limit, leading to the experimental verification of the limit behavior of the Cramér-Rao bound. Also, it was performed an analysis of each image centering algorithm applied, along with the achievement of a better understanding of the relevant aspects of the experimental setup.

A mis padres, Joel y Ana María
que me entregaron el gusto por aprender.

Agradecimientos

Agradecer a mi familia por su apoyo incondicional durante toda mi vida y especialmente en esta etapa tan importante. A mis padres Joel y Ana María, por su cariño, apoyo, contención y entrega de innumerables enseñanzas, dentro de ellas el regalo que me permitió llegar a este momento, el gusto por aprender. A mi hermano Joel, gracias por la gran ayuda en la escritura de esta memoria y a mi hermana Valentina, por su constante compañía, ambos pese a la distancia estuvieron siempre presentes entregandome mucho ánimo y cariño. A todos ustedes les debo y dedico todos mis logros.

A mi Tía Mónica, la Rosa, por todas las risas, buenos momentos y apoyo, especialmente durante este proceso. Mi prima Paulina por su gran amistad y mi abuelo Hernán, por ser mi máximo hincha durante toda mi vida. A mi Tío Luis, a quien considero mi más querido mentor. También agradecer a mi abuela Nancy, mi abuela Eugenia, mi Tía Ximena, mi prima Camila y la señora Amanda, por todo el cariño, apoyo y preocupación. A mi gata Biuti que me acompañó tantas noches de trabajo.

A mis queridas amigas Ilana, Dani Schumacher, Dani Parra y Dani Campos, sin ustedes no habría logrado llegar a este punto. Gracias por ser incondicionales, por todas esas noches de estudio, de risas, de conversaciones. Son las mejores.

A mis amigos Diego y Pipe, gracias por el apañe permanente, especialmente durante esta etapa, son lo máximo. Seba, gracias por toda tu ayuda, apoyo, cariño e infinitas enseñanzas. Nico, gracias por ser mi partner siempre. Claudio, Kaschel, Leo y Ianiv, son unos bacanes, gracias por tanto. A todos mis amigos Sumaria2, por los momentos llenos de risas y compañía. A Seba y el equipo de Handball por darlo todo, dentro y fuera de la cancha.

A mis amigos de la vida, Ale, Benja, Cami, Fefi y Xabi por estar siempre presentes. A mi amiga Laura por ser práctimente una hermana.

Finalmente, quiero agradecer a los integrantes de mi comisión, especialmente al profesor René Méndez, por brindarme su ayuda y darme tantas oportunidades y enseñanzas por las que le estaré siempre agradecida. To Mario Gai and all the members of the Astrophysical Observatory of Turin, specially to Mario Lattanzi that supported our activity and the cost of my visit, and Alberto Riva and Deborah Busonero, that made me feel welcome and made possible the development of this work. Thanks for everything.

Contents

List of Tables

List of Figures

Chapter 1

Introduction

Astronomy has marveled humanity for millennia and played a crucial role in ancient great civilizations that used it as a way to predict their fate according to the changes in the sky and to interpret the wishes of the gods. Trough the years, astronomy has evolved to its current state, where it has established itself as a science devoted to give an answer to the the greatest mysteries of the cosmos.

Initially, early astronomers utilized the naked eye to make observations of the movement of bodies in the sky, keeping records as annotations and hand-drawn diagrams. However without the aid of other instruments all objects in the sky appear to be equidistant, which was an obstacle to perform more precise observations. Later, in the early 1600s, the development of instruments such as the telescope, led to a significant improvement, allowing the observation of fainter objects and better angular resolution. Although these advances were a great enhance in the area, everything changed with the appearance of the photographic plate, which made possible to keep a detailed, permanent and quantitative record of the observations and to detect faint objects due to its ability to accumulate light over a long period of time.

With the consecutive improvements on observation technologies, every branch of astronomy enhanced their observations and data, among them, astrometry, which is the science devoted to the study and measurement of the position and motion of celestial bodies with high accuracy. This technological revolution led to a race to obtain better images with higher quality using more and better detectors.

Currently, bidimensional digital detectors are the most utilized instruments in astronomy leading to a radical change in the field, through enabling the improvement of data in several aspects, and making possible detection in different wavelengths as well as reach higher resolution. Nevertheless, a full characterization of its operation it is critical in order to determine the maximum location accuracy achievable in the measurements, being a fundamental issue on several others researches.

In this framework, Mendez et al. [2013, 2014] [1][2] developed theoretical tools based on statistical estimators that allow to determine the maximum precision achievable on ideal photometrical and astrometrical conditions, using bidimensional digital detectors. Despite the fact that previous results agree with this theoretical value for the location variance, it is necessary to perform an experimental verification.

1.0.1. Objectives

The aim of this work is to experimentally verify the astrometric Cramér-Rao limit through the comparison of the location variance obtained empirically, with the theoretical value of the Cramér-Rao variance. The adoption of this limit, enables to calculate the theoretical value for the maximum accuracy achievable, utilizing only a limited number of parameters of detector and image parameters.

For this purpose, we require an experimental setup able to simulate a set of point-like sources and then acquire several sequential images of the same trial with a bidimensional digital detector. Later, the obtained data will be analyzed, determining the maximum achievable location accuracy for each object in every used method. Finally, it will be proceed to verify the theoretical Cramér-Rao limit experimentally.

To reach this goal it would be necessary to accomplish the specific objectives that are listed below

- Design, install and align the optics of an experimental setup that allows accurate astrometric measurements with a bidimensional digital detector.
- Analyze the obtained experimental data, applying different reduction methods and image centering algorithms.
- Analyze the performance of the image centering algorithms used and the quality of the obtained data to ensure the conditions required for the study.
- Calculate the theoretical astrometric Cramér-Rao limit based on the data and detector-obtained parameters. Subsequently, compare them with the experimental results.

The study of this subject is necessary for future development of innovative astrometric applications aimed at achieving high precision measurements, extending the state of art of this branch of astronomy.

Chapter 2

Literature Review

First, it is necessary to define the theoretical foundations of the work to be carried out. For this reason, throughout this chapter we describe the operation of bidimensional digital detectors, in addition to fundamental astrometical concepts and a number of crucial estimation elements.

2.1. Bidimensional digital detectors

Initially, astronomy was developed utilizing naked eye observations and hand-drawn diagrams. Later, the development of photographic plates in the 19th century led to a complete change in the field, allowing to keep permanent and quantitative records of the celestial bodies. Even when this was a significant improvement, the instruments that made possible a big leap forward were mainly the bidimensional digital detectors.

Bidimensional digital detectors are widely used in astronomy due to its essential role in multiple applications. This photo-electronic devices detect electromagnetic radiation in the form of individual photons hitting the detector. This process generates an electrical signal that is subsequently digitized at the end of the exposure, generating a value proportional to the number of incident photons. Finally, this information is stored numerically, allowing its later computational analysis. Consequently, the measurements are quantitative and highly accurate, which allows to perform an analysis and comparison of the results objectively obtained besides the perception of the analyst.

CCD and CMOS are the two most used digital detectors. In the next section, we will describe their principal features and differences. The operation of both instruments is based on the photoelectric effect, which is the emission of electrons due to the incidence of photons on certain materials. Albert Einstein developed the theoretical explanation of this effect based on the corpuscular theory of light and the concept of *quanta*, proposed by Max Planck. He was awarded the 1921 Nobel Prize in Physics for this work. Bidimensional digital detectors make use of this principle, calculating the number of emitted electrons to determine the amount of incident photons.

2.1.1. CCD

The Charge Coupled Device, usually known as CCD, is an array of microscopic, rectangular, light-sensitive regions called pixels. This little regions are typically made of silicon.

Measuring the brightness distribution of a celestial object with a CCD can be understood with an analogy. Each pixel can be likened to a little bucket that collects the rainfall at a sector of a field. Once the rain ceased, the buckets in each row are moved horizontally one position to the right. This process is known as Parallel transport. Hence, all buckets of the last column reach a vertical conveyor belt called Serial output register. As each bucket reaches the end of the conveyor belt, it is emptied into a special bucket that measures the amount of water known as Output register. This is repeated with all the other buckets in the conveyor. Once the Serial output register is emptied, the whole procedure is repeated until all the buckets of the field are measured. In the CCD, instead of water and buckets, the things measured are photons and pixels.[3]

Consequently, we can distinguish four main stages in the CCD operation which are listed bellow

- Generation of photo-electrons.
- Collection of produced electrons.
- Charge transfer
- Readout

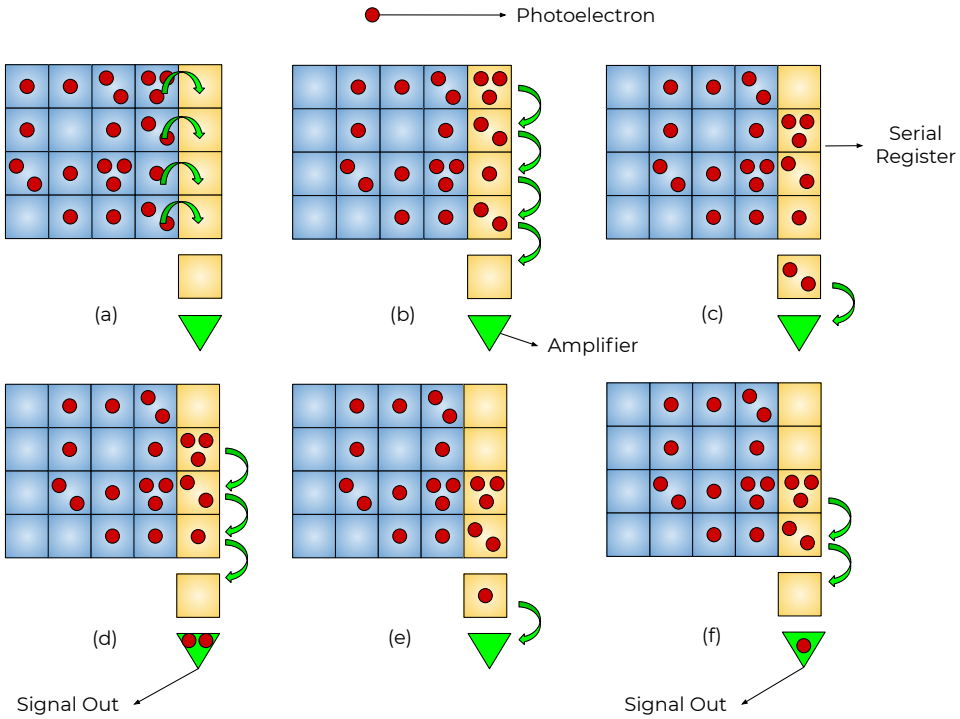

Figure 2.1: Charge transfer and readout scheme on a CCD

First, the photoelectric effect cause the emission of electrons when the incident photons coming from the source, hit the silicon array. Each pixel collects the electrons generated in this region due to the existence of a potential well produced by voltage differences. Once radiation exposure is finished and all the photo-electrons have been collected, the stage of charge transfer starts. This stage was previously explained with the analogy of water and buckets. Each row of pixels is a parallel register that moves horizontally, as shown in the figure 2.1, one position to the right. When electrons stored on each pixel of the last column reach the Output serial register, they move vertically towards the Output register, falling, one by one, on the amplifier, followed by an Analog-to-Digital Converter, known as ADC, where the readout stage begins. The ADC, converts the analog signal produced by the electrons to a digital discrete signal, known as Data Number, measured in ADU (Analog-to-Digital Unit). The accuracy of this conversion is limited by the number of bits in which the ADC can save each value. If the ADC has N bits, then the dynamic range of the signal is 2^N which is also the number that defines the pixel saturation of the detector.[4] This value is also affected by the full well capacity that corresponds to the amount of electrons than can be stored within an individual pixel. Usually the full well capacity and the saturation level are equal, but it is important to notice that the first quantity is determined by the electronics of each pixel of the detector, while the saturation level it is limited by the number of bits of the ADC.

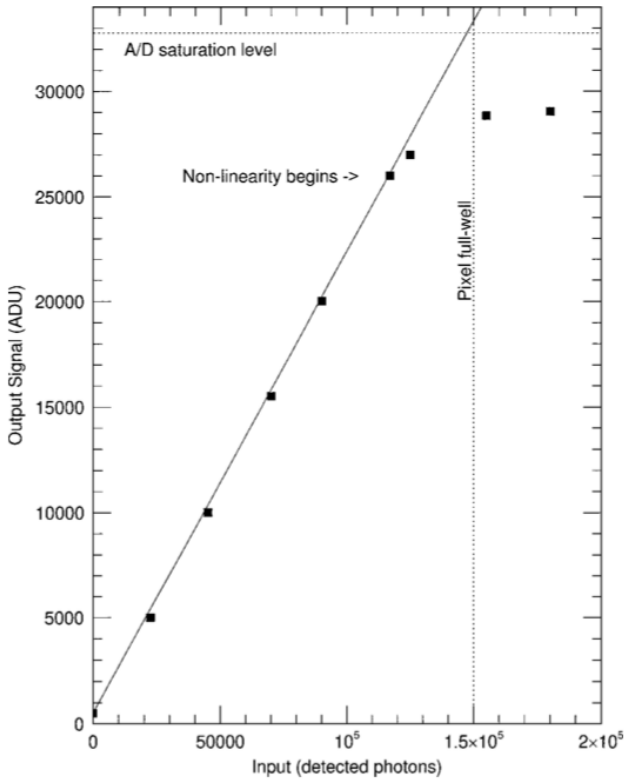

Figure 2.2: CCD linearity curve for a typical three-phase CCD as a function of the number of generated photoelectrons.

Through the previous process, an array is generated, which is the digital image, where each element represents the measured amount of counts per pixel, also know as Data Number. This is the final output of the detector.

A crucial CCD operational parameter is the gain of the detector, which is a conversion factor from photoelectrons to a digital signal measured in ADUs. This parameter corresponds to the amount of electrons represented in one ADU. The previous behavior is described in the equation 2.1, where $N(e^-)$ is the number of photoelectrons, DN the Data Number and G the gain of the detector.

$$N(e^-) = DN \cdot G \tag{2.1}$$

Because the detector only has one readout output, the gain is the same for all the pixels, and it is only determined by the electronics of the ADC. This is one of the main features of a CCD, although, it only can have small variations when it is converted to a function of the detected photons on each pixel. This can be seen in the figure 2.2, which shows the curve of obtained ADUs as a function of detected photons. During most of the considered range, the curve has a linear behavior where the slope is the gain of the detector, however, near the full well capacity of pixels, the CCD has a non-linear operation, changing the value of the slope, therefore, changing the gain value. [5]

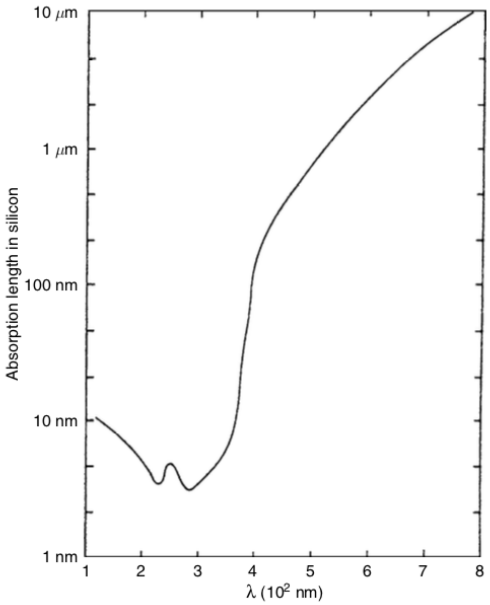

Figure 2.3: Photon absorption length in silicon as a function of wavelength in nanometers.

Additionally, the number of emitted photoelectrons also depends on an efficiency factor called Quantum efficiency, which corresponds to the ratio of photoelectrons generated and incident photons. Quantum efficiency is an equally important factor as the gain forementioned, because it gives account of the detector's performance as a wavelength function, as it is shown in equation 2.2, where $N(e^-)$ is the number of generated photoelectrons, $N(photons)$

is the number of incident photons and QE is the Quantum efficiency. This parameter is a function of the silicon thickness and the incident radiation wavelength.

$$N(e^-) = QE \cdot N(photons) \tag{2.2}$$

As figure 2.3 shows, Quantum efficiency is directly related to the photon absorption length and the incident radiation wavelength. The curve represents the absorption length, which is defined as the distance for which 68 % $(1/e)$ of the incoming photons will be absorbed. Outside the range of $3.5 \cdot 10^2$ nm to $8 \cdot 10^2$ nm the majority of photons reflect off the CCD surface, pass right through the silicon, or they get absorbed within other layer or circuitry, therefore, Quantum efficiency is critically dependent on the silicon thickness. [5]

Figure 2.3 also shows that for blue wavelengths, Quantum efficiencies are lower overall due to the tiny silicon thickness necessary to correctly perform photon absorption, being a known defect of CCDs. However, even considering this, Quantum efficiency of CCDs is considerably higher than in previous imaging devices, as is shown in figure 2.4, where it can be seen that CCDs has higher percentage values in a broader range of wavelengths. Also, Quantum efficiency can be improved for specific wavelengths during manufacturing process with coatings of different materials over the silicon chip.

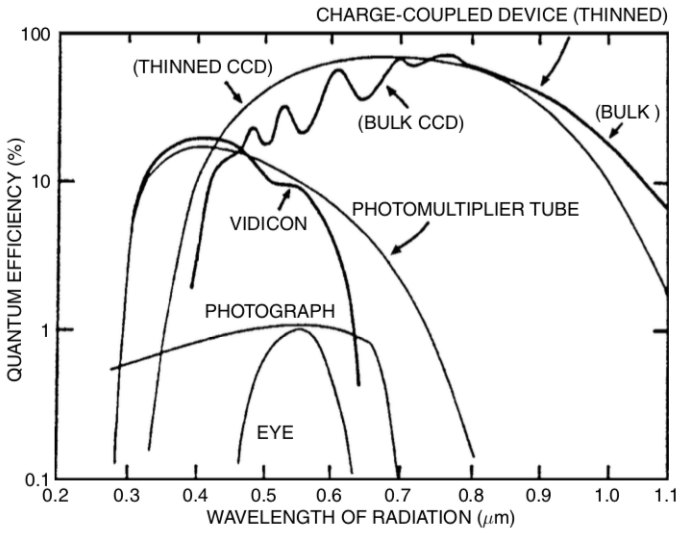

Figure 2.4: Typical Quantum efficiency for various detectors.

It can also be seen from figure 2.4 that thinned CCD's perform well at short wavelengths, corresponding to blue light. This type of CCD is also called back-side illuminated devices, because it is mounted upside down and illuminated from behind. Due to this feature, the incoming photons are directly absorbed by the silicon without interference from electronics, so the absorption length behaves as shown in figure 2.3, which exhibits that the photons are mainly absorbed over a short length of the silicon, allowing a proper operation over these wavelengths.

Another important parameter is the Charge Transfer Efficiency which is the percentage of charge correctly transferred from one pixel to another. Usually, for modern CCDs, this value is approximately 100 %, however, as the size of the pixel array increases, the charge transfer efficiency becomes increasingly important since multiple charge transfers must be made from one pixel to another in order to bring all the electrons to the ADC, especially in the farthest pixels. [5]

2.1.2. CMOS

A CMOS detector is a device based on CMOS technology, which stands for Complementary Metal-Oxide Semiconductor, that is a combination of NMOS and PMOS technology[1]. This is one of the main differences between CCD and CMOS, because CCDs only use one type of the mentioned technologies. [6]

CMOSs also use the photoelectric effect as the primary basis of their operation, nevertheless, there are important differences with CCDs. The biggest distinction is that instead of having just one amplifier, it has one amplifier for each pixel, hence, there is no need to transfer charge between pixels. This technology is known as Active Pixel Sensor. Due to the existence of independent amplifiers, the gain of the detector it is not uniform, i.e. gain it is a function of the pixel G_{ij} showing small variations, yet, for the vast majority of applications it can be considered constant.

Other important feature is that, unlike CCDs, CMOSs can be manufactured with different materials, not only silicon, which allows to increase or decrease sensibility in specific wavelengths.

2.1.3. CCD and CMOS comparison

As described in previous sections, both types of detectors have similar operations, however, CCDs and CMOSs differ in particular features that can be an advantage for certain purposes. This differences allows to select the best detector for each application.

Since every pixel has its own amplifier, characterization of CMOSs detectors is more difficult than for CCDs. At the same time, this feature makes CMOSs detectors significantly faster due its efficiency on readout process, as is shown in figure 2.5. This also, implies that CMOSs are not affected by charge transfer noise during the readout stage.

Another significant difference is the type of semiconductor material used to build the detector's chip. In the case of CMOS, it can be manufactured with another materials, not only silicon, increasing Quantum efficiency for specific wavelengths. Finally, cooling systems

[1] NMOS technology utilizes a type of semiconductor that operates using negative charges, i.e. the on and off switching of electronics is determined by the movement of electrons. In contrast, PMOS technology performs the same behavior but utilizing positive charges or holes.

aimed to reduce noise due to dark current, are usually better on CCDs.[7]

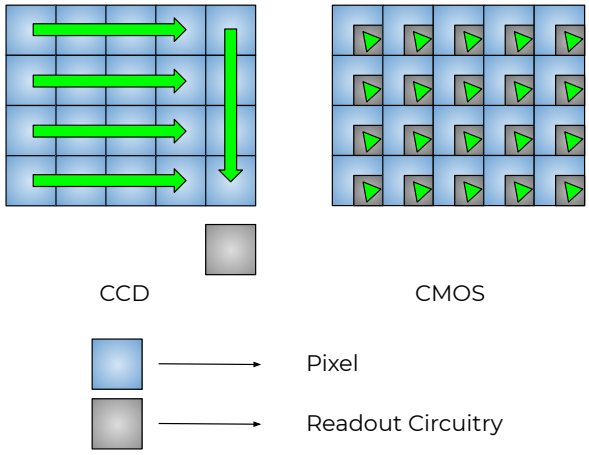

Figure 2.5: Readout comparison between CCD and CMOS.

2.2. Astrometry

Astrometry is a branch of astronomy devoted to the measurement of the position, absolute and relative, along with the motion of celestial bodies with the highest accuracy achievable.

For this purpose, electronic sensors, such as those described in the previous section, have been used to detect radiation that cannot be seen with the naked eye. In addition, it is necessary to use computerized processing of the digital images obtained, so relevant characteristics can be identified, facilitating their study. The above-mentioned technologies, have boosted the development of astrometry, which is constantly looking for new methods to increase the accuracy of the measurements.

In order to fully understand this work it is necessary to review a number of relevant astronomical and astrometric parameters within the scope of this research which are detailed in the subsections below.

2.2.1. Luminous intensity and Flux density

Assuming that there is radiation crossing a surface dA, we can consider that a part of this radiation will leave the surface within a solid angle of $d\omega$, where the angle formed between the normal of the surface and the solid angle is θ. Also, the area element is projected, obtaining $dA_n = cos\theta dA$ [8] Consequently, the amount of energy dE with frequencies between ν and $\nu + d\nu$ is presented in equation 2.3.

$$dE_\nu = I_\nu cos\theta dA d\nu d\omega dt \tag{2.3}$$

where I_ν is the specific intensity of radiation with frequency ν, in the direction of the angle $d\omega$ as is shown in figure 2.6. From now on this will be called simply intensity.

If the intensity is independent of the direction considered, dE_ν will be proportional to the area element perpendicular to radiation direction. This is called cross-sectional area.

Accordingly, the total intensity I can be defined as the integral of I_ν over all possible frequencies, as shown in equation 2.4.

$$I = \int_0^\infty I_\nu d\nu \tag{2.4}$$

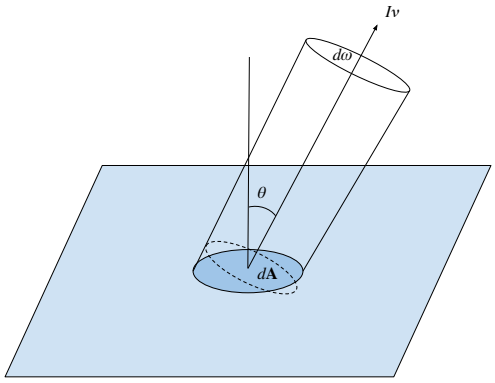

Figure 2.6: Luminous intensity I_ν of the energy crossing an area dA within a solid angle $d\omega$ in θ direction.

Usually, from an astronomy-observational point of view, the main parameter is the flux density, denoted as F_ν for a specific ν. This corresponds to the radiation power per area unit, per unit frequency, where S is the surface where the flux is measured. Typically this is considered as an spherical surface. Equation 2.5 shows the expression of F_ν.

$$F_\nu = \frac{1}{dAd\nu dt}\int_S dE_\nu = \int_S I_\nu cos\theta d\omega \tag{2.5}$$

Finally, the total density flux is obtained integrating the equation 2.5 over all possible frequencies. The result of this operation is shown in equation 2.6.

$$F = \int_S I cos\theta d\omega \tag{2.6}$$

2.2.2. Point Spread Function (PSF)

Stars are at such great distances that for all practical purposes they can be considered as point sources. However, in practice, this is not always true. This is the reason because the Point Spread Function is defined, that is to say, shows how the light from a point source spreads over multiple pixels.

The Point Spread Function, known for its acronym PSF, can adopt numerous shapes depending on the optics used and the atmospheric effects, however, is usually approximated assuming that a point source with a wavelength of λ is observed through a perfect lens with a circular aperture, resulting in a PSF limited by the diffraction of light that draws a diffraction pattern known as Airy disk .

This diffraction pattern puts a theoretical limit to the maximum accuracy achievable in object observations. For example, in the case of a telescope, an image cannot be formed as a point source, instead it appears in the form of a small circle, due to the dispersion of the light over the surface of the lens.[8]

Further, the PSF of the observed object can be calculated from the mathematical expression for the Airy disk, obtaining the result presented in equation 2.7, where $J_1(x)$ is the Bessel function of first order and first kind, and $x = \pi D sin\theta/\lambda$ where θ is the angular radius measured from the center of the aperture.[4]

$$I(\theta) = I_0 \left(\frac{J_1(x)}{x} \right)^2 \tag{2.7}$$

Due to the shape of Bessel functions, there are zones with constructive and destructive interference surrounding the central peak in the form of concentric rings, as can be seen in the figure 2.7, where the solid line represents the mentioned PSF.

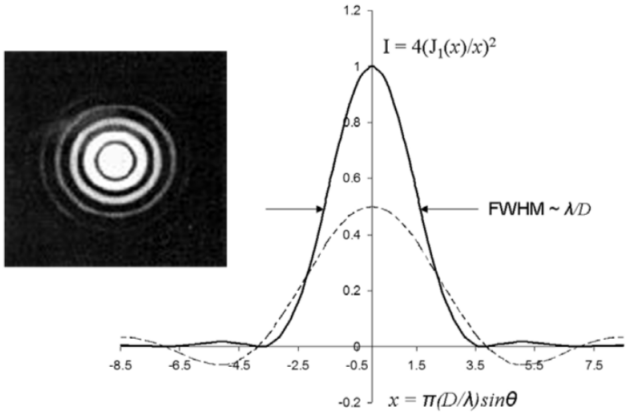

Figure 2.7: PSF of the Airy diffraction pattern for a circular aperture of diameter D

For small angles utilizing radians as units of measure, the equation 2.8 is satisfied.

$$\theta = 1.22\frac{\lambda}{D} \tag{2.8}$$

Although the theory corresponds to the Airy disk PSF, this results can be approximated to a Gaussian distribution whose shape is shown in the equation 2.9, where μ represents the center of the curve. Due to optical and atmospheric effects, it is a good approximation to consider that the PSF behaves as a Gaussian function. In the case of astrometric measurements, μ represents the position of the object to be measured. The approximation can be made in multiple other applications.

$$PSF(x) = \frac{1}{\sigma\sqrt{2\pi}} exp\left(-\frac{(x-\mu)^2}{2\sigma^2}\right) \tag{2.9}$$

2.2.3. Full Width at Half Maximum (FWHM)

Full Width at Half Maximum, abbreviated as FWHM, is a measure of the dispersion of a function. It is obtained calculating the difference of two points of the independent variable where the dependent variable has a value equal to half the maximum value of the function, as shown in figure 2.8.

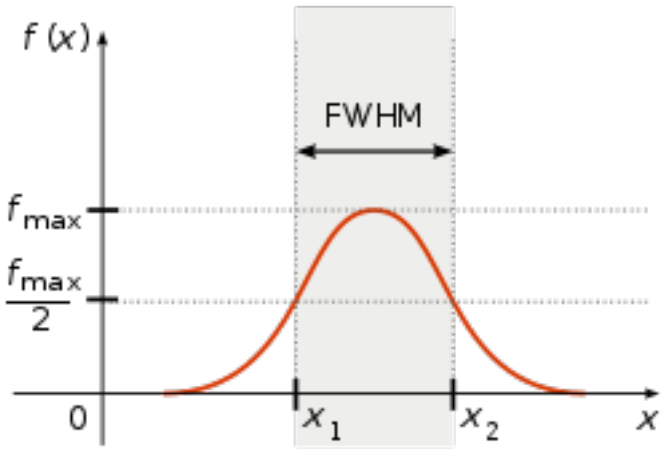

Figure 2.8: Full Width at Half Maximum of a function.

In astrometry, usually it is calculated the FWHM of the PSF, described in the previous subsection. As indicated, the most usual PSF is a Gaussian function, so it is extremely important to know the expression of the FWHM of a Gaussian function, shown in equation 2.10.

$$FWHM = 2\sqrt{2ln2}\sigma \tag{2.10}$$

2.2.4. Background

Background is the average signal per pixel at zones of the image where no stars are present. This background is the contribution of numerous noise sources, such as the variance of the readout noise, signals from unresolved sources, and light scattered by the atmosphere. It can be determined by taking the median of the values of the pixels that do not directly contain a star as a source of light.[9]

2.2.5. Signal-to-Noise Ratio (SNR)

The Signal to Noise Ratio, usually known for its acronym SNR, is a widely used quantity in science and engineering, that allows to compare the signal power and the noise power, representing the quality of the signal. It is usually measured in decibels (dB) with the expression shown in equation 2.11.

$$SNR = 10log_{10}\left(\frac{P_{señal}}{P_{ruido}}\right) \tag{2.11}$$

In astronomy, specifically in CCD detectors, the signal to noise ratio is defined as shown in equation 2.12. This is known as the CCD equation.

$$SNR = \frac{N_*}{\sqrt{N_* + n_{pix}(N_S + N_D + N_R^2)}} \tag{2.12}$$

where N_* is the total number of photons coming from the studied source, n_{pix} is the amount of pixels considered in the analysis, N_S is the total number of photons per pixel contributed by the background, also called sky, N_D is the total number of photons produced by the dark current due to the temperature of the device (even if it is small, still contributes to noise), and N_R is the noise produced during the readout process. All this parameters are measured in e^-.[5]

Generally, we measure this quantities in ADU's, so utilizing the gain G as the conversion factor, we obtain equation 2.13, where all the parameters are measured in ADU's.

$$SNR = \frac{N_*}{\sqrt{\frac{N_*}{\sqrt{G}} + n_{pix}(N_S + N_D + N_R^2)}} \tag{2.13}$$

For bright stars, since $\sqrt{N_*}$ is the dominant term in the previous expression, equation 2.12 can be approximated as shown below in equation 2.14.

$$SNR = \frac{N_*}{\sqrt{N_*}} = \sqrt{N_*} \tag{2.14}$$

It is important to consider that equation 2.14 is only valid for bright light sources where the noise is dominated by the source itself, however, for weak sources, it is necessary to use the equation 2.12 with all the corresponding noise terms.

2.3. Estimation Elements

2.3.1. Astrometric Cramér-Rao Limit

Méndez et. al. [1, 2] developed the astrometric Cramér-Rao limit which corresponds to a theoretical statistical tool that allows to calculate the minimum variance achievable for the position of celestial objects as a function of observational and instrumental parameters.

The Cramér-Rao limit has two different expressions, as is shown below in equation 2.15, depending on the regime of the observed object, i.e., if the flux dominates over background or vice versa.

$$\sigma^2_{CR} \approx \begin{cases} \frac{\sqrt{\pi}}{2(2ln2)^{\frac{3}{2}}} \cdot \frac{B}{GF^2} \frac{FWHM^3}{\Delta x} & F \ll B \\ \frac{1}{8ln2} \cdot \frac{1}{GF} \cdot FWHM^2 & F \gg B \end{cases} \tag{2.15}$$

In the equation above, F is the flux of the object, B is the background, $FWHM$ is the full width at half maximum of the PSF of the studied object, G is the gain of the detector and Δx is the size of the pixel.

This theoretical limit does not depend on the size of the array of pixels if the PSF is well sampled.

2.4. State of art

The interest in determining the maximum precision achievable obtained in both, theoretical and experimental astrometric measurements, has been a very important issue in the development of astronomy, since the reliability of the conclusions obtained from the data depends on how well characterized are the sources of error involved, along with other procedures to eliminate their effects.

The determination of the variance of the data and their effects also allows to design new technologies and experiments that can help to increase, even more, the accuracy of measurements and images in astrometry. Those improvements contribute to the development of this field of study.

In this framework, numerous investigations have been developed to determine and improve the behavior of the data variance. This effort is divided in two different branches, the first one aims to elaborate and enhance image centering algorithms utilizing multiples methods, while the second, is devoted to designing and implementing new experiments to characterize different devices and their achievable accuracies.

The work elaborated by the Local Cosmology group at the Turin Astrophysical Observatory it is contained in the second area of research. The project consisted in an experimental setup, shown in figure 2.9, that allowed to study how the position of celestial objects varies through a set of sequential images of the same experiment.[10]

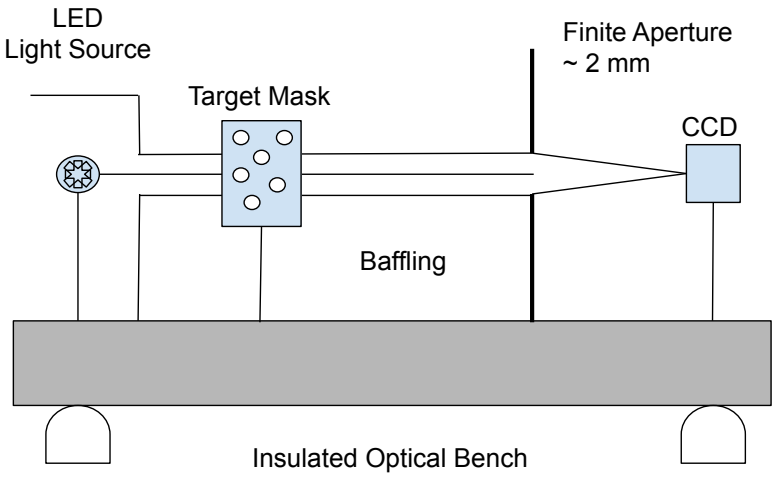

Figure 2.9: Experimental setup designed and implemented by the Local Cosmology group at the Turin Astrophysics Observatory.

This study, with first experimental results published in 2001, is the main basis for the project presented here.

In addition, the development of new image centering algorithms has been approached by numerous researchers, applying various techniques as the Gaussian fit, the maximum likelihood method [11] and even a new method with Bayesian routine [12]. Furthermore, research has been carried out to study the performance of algorithms dedicated to the estimation of different measurement parameters [13]. All this researches allow to continually expand this area of astronomy, improving the measurements and methods utilized, reaching higher accuracy levels.

Chapter 3

Methods

In the previous section we presented the theoretical foundations necessary to understand the operation of bidimensional digital detectors and the astrometric, optic and statistical parameters. Now, it is possible to start the next chapter where we will study the methods and procedures made through this work.

First, we will study in detail the setup, design and implementation of the experiment performed during this work in order to take precise astrometric measurements with a bidimensional digital detector. Later, we will discus the image centering algorithms operation and coding. This algorithms were utilized for the analysis of the data. Finally, we will review the necessary procedures to calculate the experimental and theoretical Cramér-Rao astrometric limit.

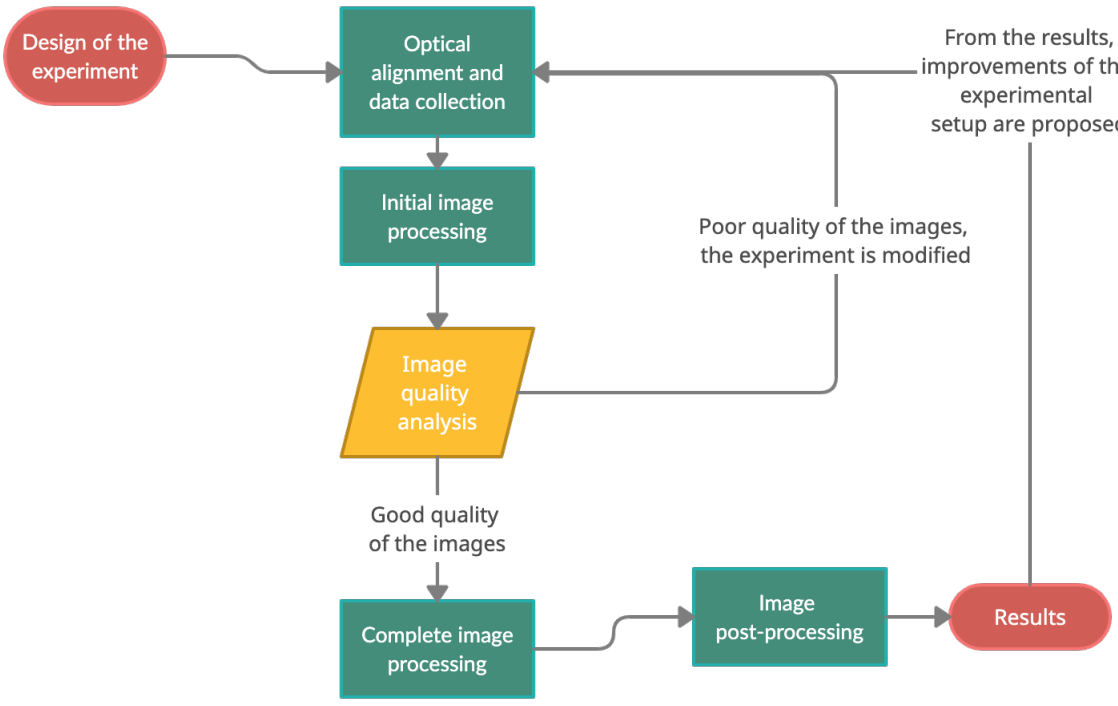

Figure 3.1: Flow chart of the methodology

Even if all these steps are described sequentially, where the results of one stage affected the development of subsequent and previous activities of the methodology, several iterations were made. This relation between the stages of the experimental setup is shown in figure 3.1.

Firstly, the experimental setup was designed and subsequently implemented, aligning the optical components. Later, the data was collected and the images were initially processed. Where the quality of the obtained image was poor, the experimental setup was modified and all the previous stages were repeated. On the other side, where no image problems were observed, the experiment proceeded to the final part of the image processing and post processing. Finally, from the results, improvements of the experimental setup were proposed.

3.1. Design and implementation of the experimental setup

As described earlier, the first stage of the methodology was the design and implementation of the experimental setup, aiming to obtain sequential measurements of not resolved point-like sources utilizing a bidimensional digital detector. This allowed to capture several realizations of the same test. Later, with the obtained data, we studied the position variance for each point-like source, determining their maximum experimental precision achievable.

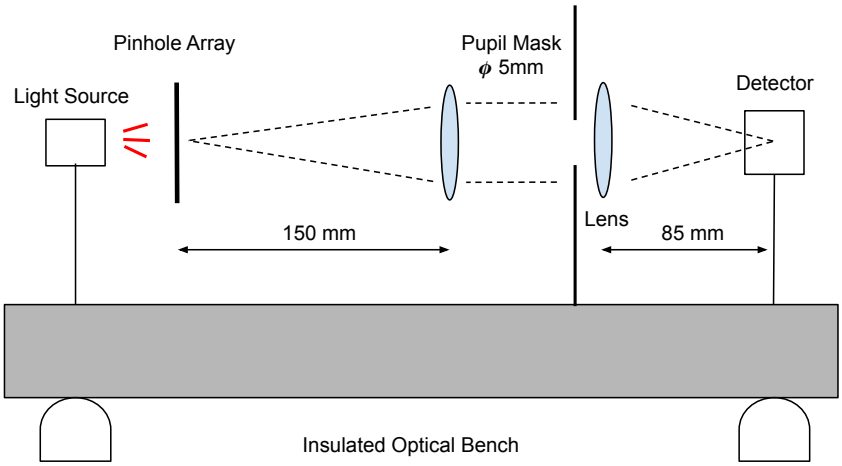

Figure 3.2: Designed and implemented experimental setup

Based on the experiment carried out by Mario Gai et al. [10] presented in figure 2.9, the experimental setup of figure 3.2 was designed utilizing the optical components listed below.

- A light source, specifically, a LED, emitting red light (625 nm) with optimized thermal properties to maintain stable power. Corresponds to Thorlabs M625L4. Further specifications are presented in table 3.1 [14] and in figure 3.3 where the normalized intensity of the light source is presented.

Table 3.1: Collimated LED Specifications

Color	Red
Nominal Wavelength	625 nm
Bandwidth (FWHM)	17 nm
Emitter Size	1 mm x 1 mm
Maximum Current (CW)	1000 mA
Forward Voltage	2.5 V
Electrical Power	2500 mW
Typical Lifetime	$\geq$ 100 000 h
Operating Temperature (Non-Condensing)	0 to 40 ºC
Storage Temperature	-40 to 70 ºC
Risk Group	RG2 - Moderate Risk Group

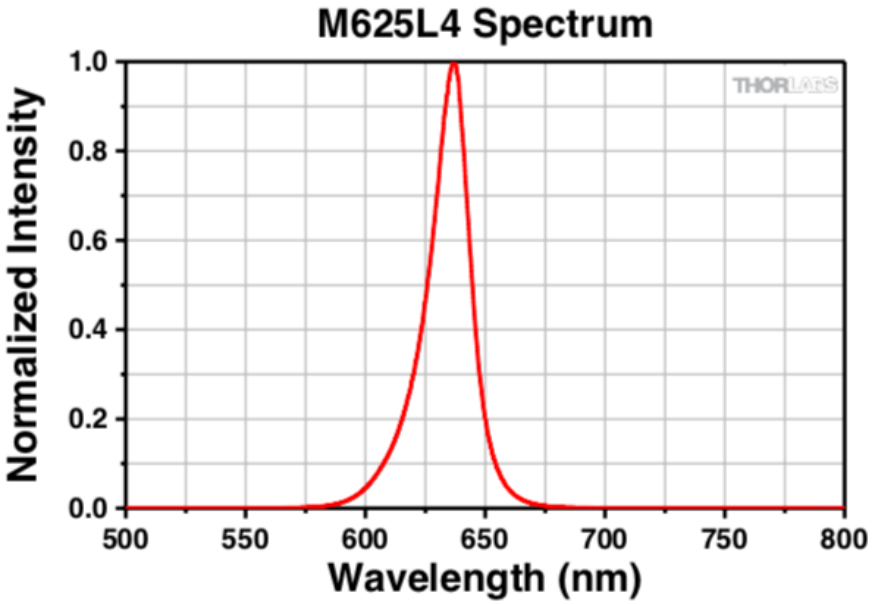

Figure 3.3: Normalized LED Intensity

- A pinhole array with 9 small holes of different sizes that allows to create point light sources that simulate the stars captured by the detector.
- A pupil mask and a lens that allow to have a collimated front, which properly focused on the focal plane of the detector.
- A CMOS detector, specifically the Kiralux 2.3 Megapixel Monochrome CMOS Camera with USB 3.0 Interface from Thorlabs. It is a 1920 x 1200 pixel array whith each squared-shaped region of 5.86μm x 5.86μm. It has a Quantum efficiency of approximately 78 % at the wavelength of 500 nm as shown in figure 3.4. Also with fanless passive thermal management that reduces the effect of dark current without adding vibration or image blur and with electronic global shutter. [15]

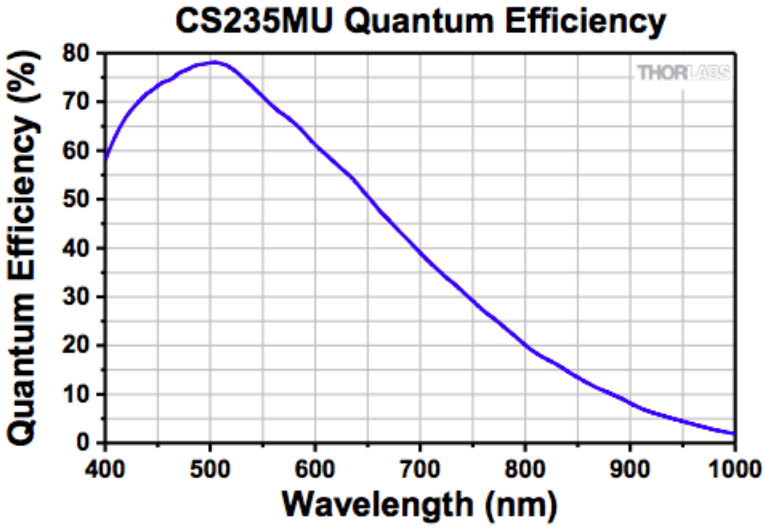

Figure 3.4: Quantum efficiency of Kiralux 2.3 Megapixel Monochrome CMOS Camera from Thorlabs

As shown, we used a 625 nm wavelength source emitting light, so the Quantum Efficiency of the detector was approximately 58 %.

Further sensor and imaging specifications are shown in table 3.2 and table 3.3. [15]

Table 3.2: CMOS Sensor Specifications

Sensor Type	CMOS Monochrome
Number of Active Pixels	1920 (H) x 1200 (V) ($\sim$ 2.3 MP)
Pixel Size	5.68 μm x 5.68 μm
Optical Format	1/1.2" Format (11251 μm x 7032 μm)
Peak Quantum Efficiency	78 % at 500 nm
Dynamic Range	Up to 75dB
Full Well Capacity	$\geq 30.000e^-$
Shutter Type	Global

Table 3.3: Imaging Specifications

Exposure Time	0.034 to 15167 ms in $\sim$ 0.020 ms Increments
ADC Resolution	12 Bits
Vertical and Horizontal Hardware Binning	1 x 1 to 16 x 16
Region of Interest (Width x Height) (For Binning at 1 x 1)	92 x 4 Pixels to 1920 x 1200 Pixels, Rectangular
Read Noise	$<$7.0 e^- RMS
Overlapped Exposures	Frames per Trigger = Continuous Only

In the star field simulator, the pinholes have been manufactured by photo-lithography and their size is of the order of $10 - 30\mu$m, which is variable because of manufacturing tolerances (custom process). Pinholes are transparent dots set on an opaque coating on an optical flat. The optical system must produce unresolved images on the detector in order to preserve the sampling of nearly diffraction limited images, i.e. photon distributions close to the PSF. Since the pixel size is about 6μm, the optical system magnification must reduce the source size by a factor 3-5. It is convenient to use a (nearly) collimated beam in the intermediate section between source and camera sub-systems, in order to allow for more freedom in experiment layout on the optical bench. Therefore, the focal lengths of collimator and camera must differ by a comparable factor 3-5.

The practical solution implemented uses a $75mm$ (3 inch) diameter doublet as a collimator, with a clear aperture of $50mm$ and a focal length of $600mm$. It is placed at $600mm$ from the light source in order to produce the desired collimated beam. The distance to the camera sub-system is then mostly irrelevant, but it is set to $600mm$ in order to allow for easy insertion e.g. of devices for modulation of the wavefront in future tests. The camera optics is a doublet with focal length set to $135mm$, in order to achieve the desired (de-)magnification factor of about 1/4. The clear aperture is set to $3mm$ in order to generate well sampled images on the detector.

The experimental setup was implemented at a clean dark room at the Astrophysical Observatory of Turin, in order to minimize the dust that could cause unwanted imperfections and aberrations on the optics, as well as to reduce the contribution of other light sources that could compromise the measurements, and also, to minimize the environmental noise, e.g. vibrations and thermal excursion. Also, the temperature of the room was stable overall due to the conditions and isolation of the room. As a result, this experiment allows to fulfill the above discussed requirements, enabling to obtain clean sequential images of 9 point-like sources of different intensities.

In order to replicate the experiment, most of the equipment a researcher would need is comparably easily procured: an optical bench and a set of off-the-shelf components (lenses, light source) represent large part of the optical system. The detector may be a more relevant element, depending on the goal of testing CCD or CMOS devices, and the need to test parameters more or less similar to those of real science instruments. A quiet operating environment may be convenient to reduce the noise on the measurements. The only custom part is the pinhole array generating the simulated star field. This may require some effort in procurement, not so much because of particularly critical requirements, but mainly because it is necessary to convince an optical component manufacturer to produce a prototype according to specifications, without the perspective of mass production, and possibly at a cost accessible to research funding levels.

3.2. Measurements

Once the experimental setup was implemented we could start the data collection stage. For this purpose, we used the ThorCam software, specifically designed by Thorlabs to control the CMOS detector.

This software was installed on a computer with Windows as operating system in order to fulfill the recommended system requirements, and connected to the detector via USB.

Once the detector was connected to the computer and the software was run, a window appeared showing the recognized camera, and its correct operation. Following, Live Window emerged, which is the main window for the camera control which displays the images obtained. This window was used to check if the optics were correctly aligned, verifying that the image of the star field was inside the pixel array and well-focused, and to check if the light source LED was calibrated to reach a near-saturation value of pixels, before taking the measurements.

The next step was to access to the Camera Settings window where some settings, as the exposure time, can be adjusted. In this case, the exposure time was fixed at 100 ms with a rate of 1 frame per second with a total of 100 frames. The resulting efficiency is of about 10 %, limited by download constraints. The rest of the settings were left at their default values, including the gain of the detector, set at 0dB [16].

This measurements were saved at a chosen folder in a TIFF format file, using the full size of the image, i.e. 1920 x 1200 pixels, as shown in table 3.3.

3.3. Data processing with image centering algorithms

In order to determine the position of the studied objects, the data was analyzed using several image centering algorithms coded with Python. This allowed to locate the centroid of the simulated celestial objects.

A fundamental aspect of this analysis was that the image centering algorithms were used over a small portion of the full measured image. A small cutout was made around each point-like source, usually of a size between $7x7$ pixels and $20x20$ pixels, which size in each case was determined by the dimensions of the studied object and its characteristics. This region is known as Region of Interest.

3.3.1. Center of Gravity

The Center of Gravity algorithm consists in estimate the position of the centroid through the calculation of the center of mass of the object utilizing equation 3.1.

$$C.O.G. = \frac{\sum_{i=1}^{n} m_i \cdot x_i}{\sum_{i=1}^{n} m_i} \tag{3.1}$$

where m_i is the intensity value on the i-th pixel, i.e. I_i from equation 2.4, and x_i is the coordinate of the pixel. Therefore, the center of mass of each point-like source is calculated and used as its respective position. This is calculated for each star on each sequential image

(also called frame) and on each axis, in order to determine how the position of the center of mass varies throughout the data set, and finally this will allow to calculate the standard deviation of the position.

3.3.2. Gaussian Fit

This method consists in fitting a Gaussian distribution, shown in equation 3.2, to the PSF of the point-like source on the Region of Interest for each star on each frame that matches the images in the least square sense. From this curve it is possible to acquire the center of the peak μ, which corresponds to the position of the point-like source, as well as study how the position varies throughout the data set. This allows to calculate the standard deviation of the position.

$$f(x) = \frac{1}{\sigma\sqrt{2\pi}} exp\left(-\frac{(x-\mu)^2}{2\sigma^2}\right) \tag{3.2}$$

In this case, we utilized the Gaussian function in two dimensions, shown in equation 3.3.

$$f(x,y) = A \cdot exp\left(-\left(\frac{(x-x_0)^2}{2\sigma_x^2} + \frac{(y-y_0)^2}{2\sigma_y^2}\right)\right) \tag{3.3}$$

3.3.3. Fit utilizing an Airy function

This method corresponds to adjusting an Airy function in two dimensions, to the detected PSF of the point-like source on the Region of Interest, just as shown in equation 3.4, for each star in each frame. After running the algorithm, an Airy function that adjusts the data in the best way possible is obtained. From this, the position of the center of each axis (x_0, y_0) is acquired, which corresponds to the position of the point-like source. Finally, the standard deviation for each star center on each axis is calculated.

$$f(r) = A \cdot \left(\frac{2J_1\left(\frac{\pi r}{R/R_z}\right)}{\frac{\pi r}{R/R_z}}\right)^2 \tag{3.4}$$

where J_1 is the first order Bessel function of the first kind, r is radial distance from the maximum of the Airy function which corresponds to $r = \sqrt{(x-x_0)^2 + (y-y_0)^2}$, R is the input parameter and $R_z \simeq 1.2197$ is a convenient starting value adjusted on a data set.

3.3.4. Maximum Likelihood

This is the last algorithm used through the analysis of this data and applies a Maximum Likelihood approach in the simple least squares sense, i.e. without weighting by the expected data variance. This method finds a solution that minimizes the sum of the squared differences between the samples and the values of a chosen model. The models for this case were the Gaussian function shown in equation 3.3 and the Airy function shown in equation 3.4.

Later, a two step approximation is used, searching for the minimum squared error on a grid of pre-selected positions. Based on this values, the position of the point-like sources are acquired. Finally, the standard deviation of the center of each star on each axis is calculated.

3.4. Data Post-processing

3.4.1. Barycentric Coordinates

After processing the data set with each image centering algorithm previously described, the post-processing is ready to start.

First, the mean of the position of all the point-like sources on each axis is computed. Next, the difference between this point and the position of each star on each frame is calculated. With this process the coordinates are referenced to the relative center of the stars, so the small changes or movements that change the positions of all stars at the same time are corrected, cleaning the data. This allows to reach higher precision when the center of the stars is determined, since the relative 'motion' of each star with respect to the collective average position is smaller than the common mode variation. This procedure is repeated on every frame of the data set. This approach corresponds to a sort of pointing error correction.

3.5. Computation of Cramér-Rao limit

Based on the characteristics of the utilized detector and the data measured, it is possible to know all the terms necessary to calculate the theoretical astrometric Cramér-Rao limit. Therefore, using the equation 2.15 as required, the predicted theoretical variance for the position of each point-like source was obtained.

For this purpose it was necessary to utilize the gain of the detector in e^-/ADU's (Electrons / Analog-to-Digital Units). To convert this quantity from dB to e^-/ADU, it was required to know the Saturation level and the number of bits of the ADC. As discussed above, the Saturation level and the Full Well Capacity are usually equal, therefore the latter quantity can be used instead. For this reason, we used the Full Well Capacity and the number of bits of the ADC, which was $30.000e^-$ in this case, according to table 3.2, and 12 bits, according to table 3.3, respectively.

As shown in Chapter 2, the pixel saturation value in this case was $2^{12} = 4096$ ADUs, the-

refore through calculating the proportion between $30.000e^-$ and 4096 ADUs, it was possible to know the ADUs number per $1e^-$. This value was the gain of the detector in e^-/ADU. Calculating, we obtained a gain of 7.324 e^-/ADU, which give us the value used to calculate the theoretical astrometric Cramér-Rao limit.

At the same time, utilizing the previously described algorithms, it was possible to calculate the experimental variance of the position of the point-like sources. Then, a comparison of the theoretical and experimental values obtained was made, with the caution that the model is necessarily simple, and it may not include unknown sources of experimental disturbances. The comparison may therefore put in evidence some of such unknown perturbations.

Chapter 4

Results

Through the last chapters, the theoretical basis and the methodology of this work have been presented. This chapter shows the obtained results and the processing of the measurements.

The studied data set consisted of 100 frames with images of 9 point-like sources of different intensities, due to the different sizes of the holes in the pinhole array and illumination geometry.. During this work we will use the term *Stars* to refer to the point-like sources whose distribution on the full image of 1920 x 1200 pixels, is shown in figure 4.1 where Star 1 is the brightest and Star 9 is faintest.

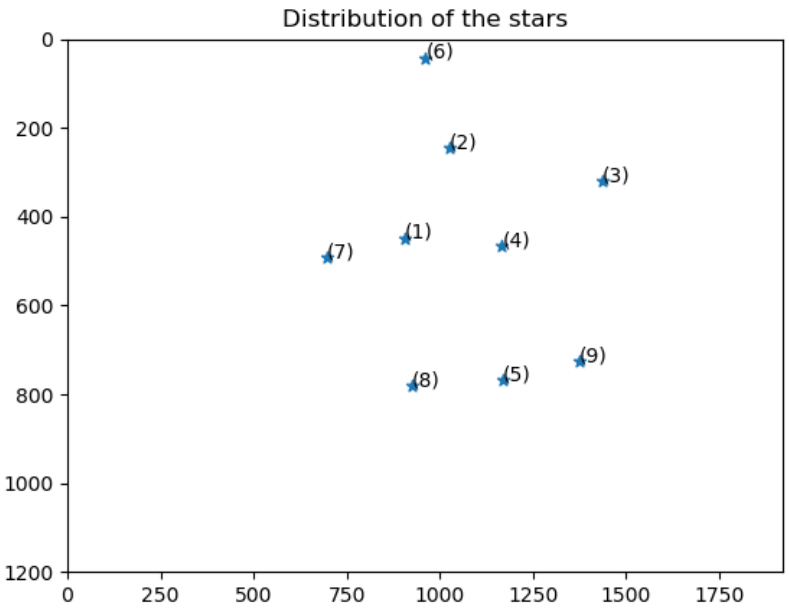

Figure 4.1: Distribution and labels of the stars on the data set

The measurements were obtained utilizing the experimental setup described in the previous chapter, using the CMOS detector with an aperture reduced to its minimum value, of approximate 1 mm, and an exposure of 100 ms with a rate of 1 frame per second (observing

efficiency 10 %). The small aperture generates a nearly aberration free image for each source on the focal plane.

The stars were analyzed utilizing a ROI (Region of interest) of 21x21 pixels, except in the case of the fit with an Airy function method and the Maximum Likelihood method with an Airy function a model, were a ROI of 20x20 pixels was used. In figure 4.2 we show the images of the individual stars as recorded on the detector utilizing a ROI of 21x21 pixels where we can see the well sampled point-like sources.

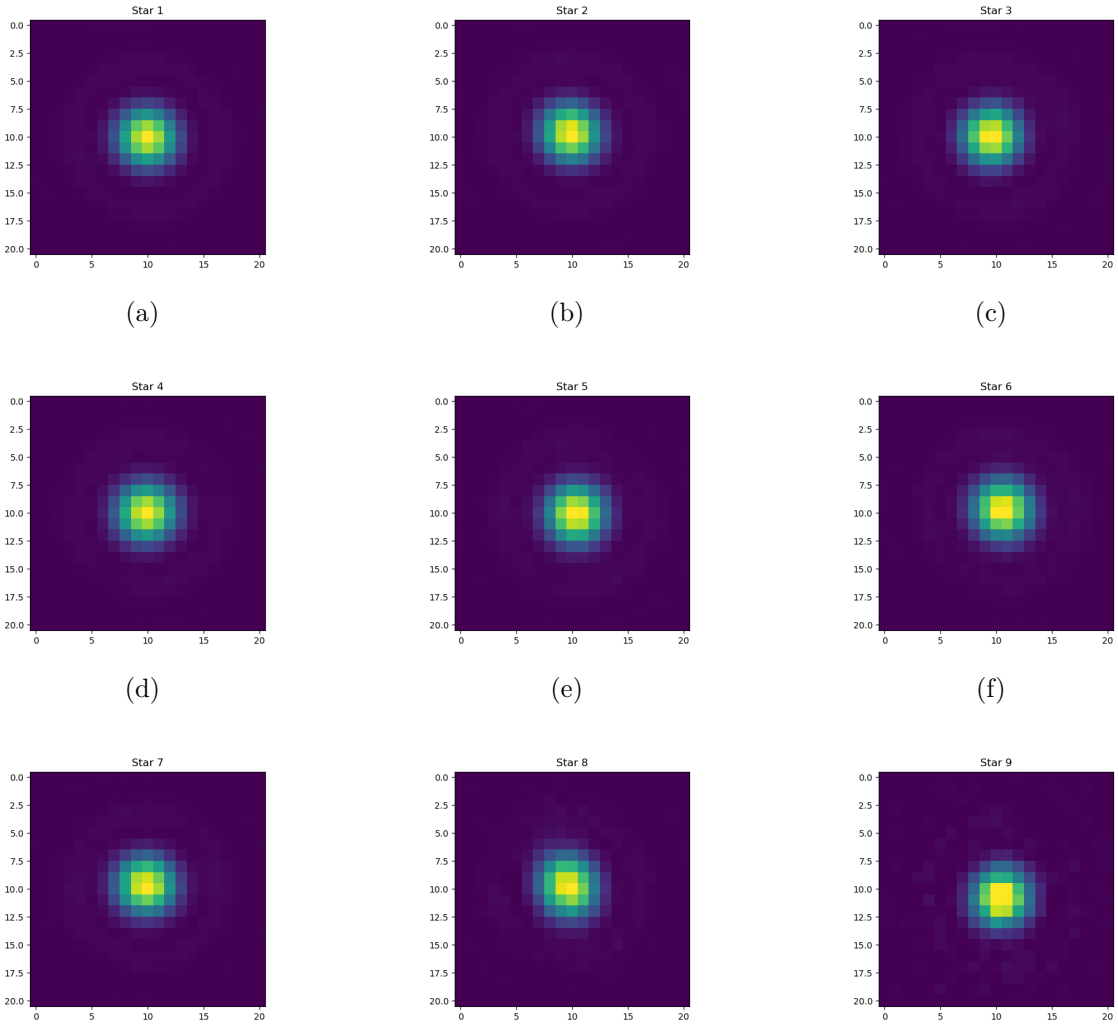

Figure 4.2: Images of the individual spots (Artificial stars) as recorded on the detector (raw 12 bit data)

Later, we applied natural logarithm over the ROI to evidence the diffraction rings. The results are shown in figure 4.3. As explained in Chapter 2 the diffraction pattern appears due to the distribution produced by the diffraction of light when a focused spot of light is observed through a perfect lens with a circular aperture.

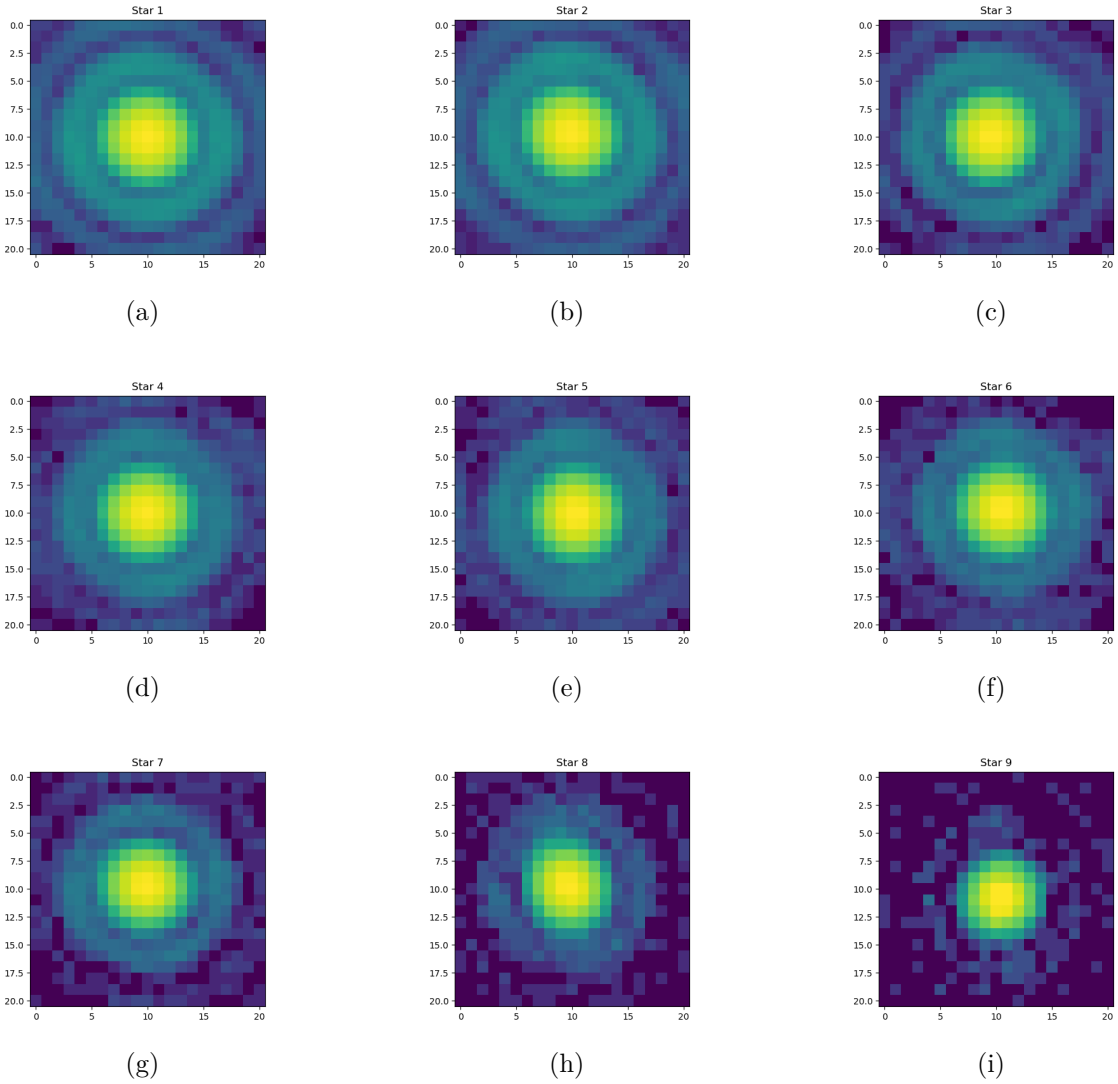

Figure 4.3: Images of the individual spots (Artificial stars) with natural logarithm applied to evidence the diffraction rings

The appearance of the diffraction pattern, in this case known as Airy disk, helps to confirm that the observed point-like sources are sufficiently well focused and representative of a near-diffraction limited telescope.

Finally, to end the initial analysis, table 4.1 shows the SNR and the maximum pixel value of each star.

Table 4.1: SNR and Maximum pixel value of the stars

Star	SNR	Maximum Pixel Value
1	740.5691	3873
2	688.0629	3271
3	464.2402	1502
4	433.3354	1316
5	411.3595	1148
6	335.1208	771
7	297.5270	657
8	184.4316	269
9	92.9352	96

The SNR was calculated using equation 2.13, where the first step was to define an aperture on the image (not to be confused with the aperture of the optical system) over which calculate the necessary parameters. For this purpose, the FWHM of each star was computed, yet the mean of this quantity was used as the final FWHM. Later, assuming that the PSF was a Gaussian distribution, the equation 2.10 was used to obtain σ the Gaussian width parameter. Finally, the aperture was defined as an interval of 3σ from the central pixel (maximum valued pixel) which corresponds to a region of 13x13 pixels that includes 99.7 % of the Gaussian distribution .

The total number of photons coming from the source was calculated adding all the intensities values of the pixels over the aperture, after subtracting the background. The background was calculated as the mean over a region of the image without point-like sources, in this case we considered the region between pixels 930 and 1200 on the Y coordinate and between 1500 and 1920 on the X coordinate. This was also the value considered for the total number of ADUs contributed by the background N_D

The total number of pixels n_{pix} is 169 due to the size of the aperture considered of 13x13 pixels. The total number of ADUs produced by the dark current was neglected due to its small value. Finally, the readout noise was obtained utilizing the gain as a conversion factor over the value shown in table 3.3.

With all this components, the SNR of each star was calculated and is shown in table 4.1.

This was the final step of the initial analysis of the data, then the different image centering algorithms were applied, starting with the Center of gravity algorithm.

4.1. Center of Gravity

The first image centering algorithm applied to the data was the Center of Gravity. This algorithm allowed to find the position of the centroid of each star in each frame for each axis. The results are shown in figure 4.4.

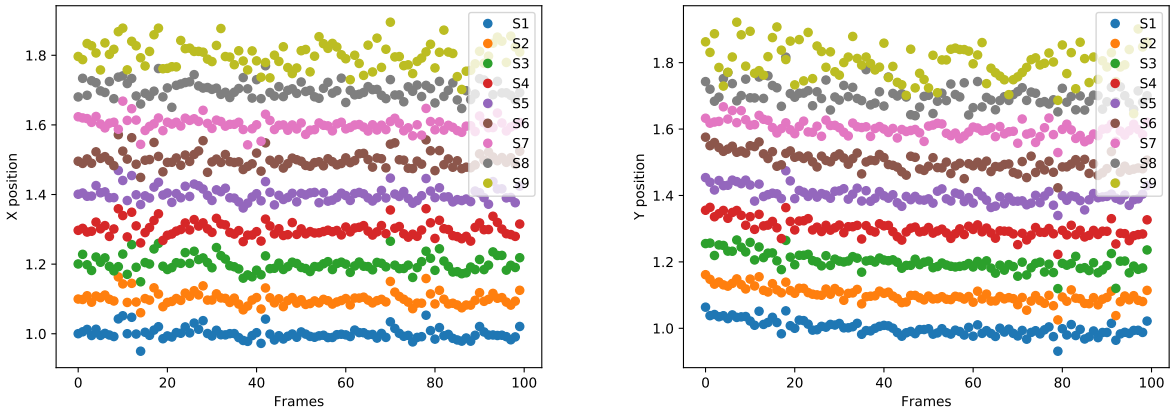

(a) Centroid of stars on X axis

(b) Centroid of stars on Y axis

Figure 4.4: Centroid of stars over the 100 frames

Figure 4.4a shows that the position of the centroids on the X coordinate are roughly stable, with small jumps of all the stars around frame 15, 40 and 80. Figure 4.4b shows that a remarkable slope is present over the initial frames on the Y coordinate, and as the other axis, exhibits small jumps of all the stars around frame 18, 36 and 80. The common mode displacement of the photo-center appears to be a mechanical disturbance of the optical system alignment, similar to a pointing error in real telescopes. Furthermore, it is notable on both axes that the position of the centroid of the fainter stars are more scattered, while for the brightest stars are more stable, showing an indirect proportion between SNR and scattering.

Table 4.2: Standard deviation of the stars position calculated with Center of mass method

Star	X Standard Deviation [px]	Y Standard Deviation [px]	X Pixel Fraction [px^{-1}]	Y Pixel Fraction [px^{-1}]
1	0.01662	0.02145	60.1685	46.6200
2	0.01810	0.02270	55.2486	44.0529
3	0.02176	0.02604	45.9559	38.4025
4	0.02025	0.02450	49.3827	40.8163
5	0.01942	0.02220	51.4933	45.0450
6	0.02202	0.02746	45.4133	36.4166
7	0.01893	0.02203	52.8262	45.3926
8	0.02303	0.03116	43.4216	32.0924
9	0.03730	0.05296	26.8097	18.8822

Table 4.2 shows the standard deviation of the position of the centroid on each axis for all the stars. Also, it shows the equivalent pixel fraction. This parameter corresponds to $1/\sigma$, where σ is the standard deviation. This variable is present as a way to improve the visualization of the data, for example, star 1 reaches a position accuracy of approximately $\frac{1}{60}$ of the size of a pixel in the X axis.

The standard deviation is measured in portion of a pixel, which is represented by [px], while the pixel fraction is measured in [px^{-1}].

Also, table 4.2 shows the same relation between SNR and scattering previously described. Besides, it can be seen that the standard deviation of the star with bigger SNR is clearly smaller in the X coordinate, approximately 1 % of a pixel, while in the case of the Y coordinate, it is around 2 % of a pixel.

4.1.1. Post-processing: Barycentric Coordinates

Once the image centering algorithm is applied to the data, the post-processing stage is ready to start.

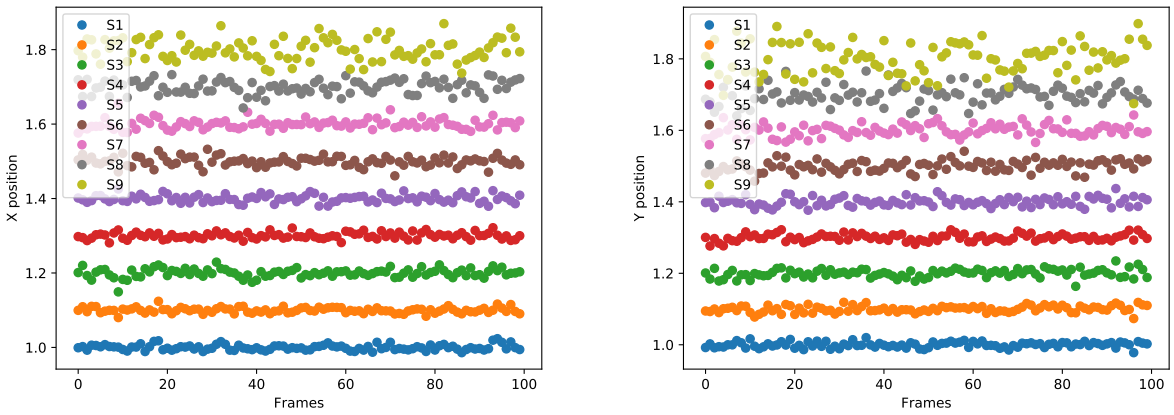

(a) Centroid of stars with Barycentric coordinates on X axis

(b) Centroid of stars with Barycentric coordinates on Y axis

Figure 4.5: Centroid of stars with Barycentric coordinates over the 100 frames

Figure 4.5 shows the results of applying Barycentric coordinates over the previously found data. It can be seen that the relation between SNR and scattering is still present i.e. higher SNR is associated to lower scattering, but the common mode of the stars on specific frames have been completely corrected on both axes, achieving more stability. In addition, the slope present in figure 4.4a has been fully erased after the post-processing of the data, as shown in figure 4.5a.

Table 4.3 shows the standard deviation and the pixel fraction of all the stars on both axes after the post-processing stage. It can be seen that the standard deviation decreases for all the stars compared to the data shown on table 4.2, reaching standard deviations of approximately 0.7 % of a pixel on both axes. In other words, the pixel fraction increases reaching an accuracy of $\frac{1}{134}$ of the size of a pixel, which corresponds to approximately 0.042μm.

Table 4.3: Standard deviation of the stars position calculated with Center of mass method and Barycentric coordinates

Star	X Standard Deviation [px]	Y Standard Deviation [px]	X Pixel Fraction [px^{-1}]	Y Pixel Fraction [px^{-1}]
1	0.00746	0.00754	134.0483	132.6260
2	0.00706	0.00890	141.6431	112.3596
3	0.01143	0.01132	87.4891	88.3392
4	0.00830	0.00948	120.4819	105.4852
5	0.00979	0.01198	102.1450	83.4725
6	0.01250	0.01512	80.0000	66.1376
7	0.01297	0.01626	77.1010	61.5006
8	0.01817	0.02577	55.03577	38.8048
9	0.02877	0.04418	34.7584	22.6347

4.1.2. Standard Deviation through frames

Another interesting feature to study is how the standard deviation for each star changes as more frames are considered in the calculation. This results are shown in figure 4.6 for both axes.

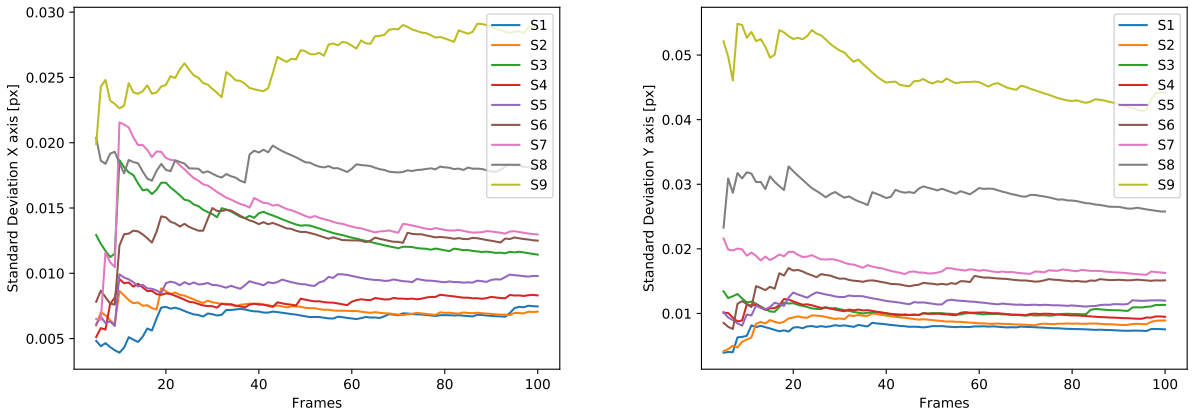

(a) Standard deviation through frames on X axis

(b) Standard deviation through frames on Y axis

Figure 4.6: Standard deviation through frames utilizing Center of gravity method and Barycentric coordinates

Figure 4.6 shows that the two stars with lower SNR need more frames to reach a more stable value for the standard deviation, in fact, star 9 does not reach an stable value over the whole set of 100 frames. On the other hand, the seven stars with higher SNR present a roughly stable value after frame approximately 70 for figure 4.6a, and after frame approximately 65 for figure 4.6b.

4.1.3. Standard deviation with different apertures

Finally, the effect of the aperture radius over the standard deviation of the stars is studied. The results are shown in figure 4.7

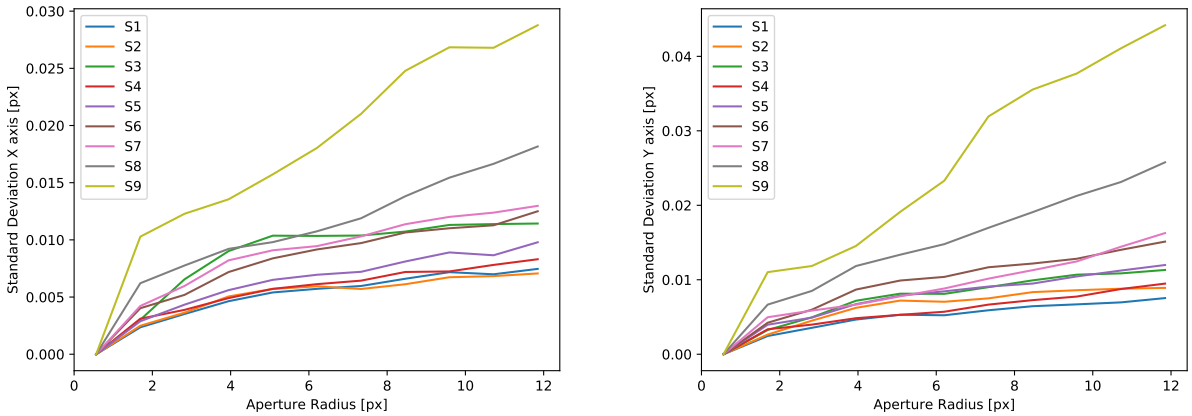

(a) Standard deviation with different apertures on X axis

(b) Standard deviation with different apertures on Y axis

Figure 4.7: Standard deviation with different apertures utilizing Center of gravity method and Barycentric coordinates

Figure 4.7 shows that both axes have a similar behavior, where in the case of the stars with lower SNR the standard deviation grows with a bigger slope as the aperture radius increases, while for the stars with higher SNR, the standard deviation changes slowly as the aperture radius grows.

Also, it can be seen that the standard deviation does not reach a stable value for any aperture radius. Since the images are well focused, additional side pixels mainly add to the noise, but for bright stars the central peak is dominant.

4.2. Gaussian Fit

The next image centering algorithm applied to the data was the Gaussian fit, whose results are shown below. All the previous analysis already described for the Center of gravity method were applied here.

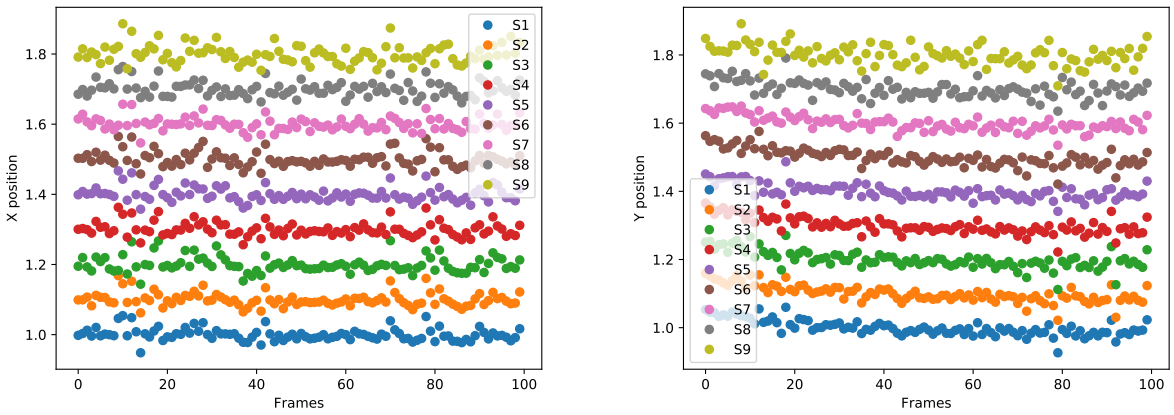

(a) Centroid of stars on X axis

(b) Centroid of stars on Y axis

Figure 4.8: Centroid of stars over the 100 frames

As the previous algorithm, figure 4.8a shows that the position of the centroids on the X coordinate are roughly stable, with small jumps of all the stars around frame 15, 40 and 80. Figure 4.8b shows that a remarkable slope is present over the initial frames on the Y coordinate, and as the other axis, exhibits small jumps of all the stars around frame 18, 36 and 80, i.e. figure 4.8 shows a similar behavior to figure 4.4, but it is more stable, specially for the stars with lower SNR. Furthermore, it is notable the same relation between SNR and scattering.

Table 4.4: Standard deviation of the stars position calculated with Gaussian fit

Star	X Standard Deviation [px]	Y Standard Deviation [px]	X Pixel Fraction [px^{-1}]	Y Pixel Fraction [px^{-1}]
1	0.01739	0.02265	57.5043	44.1501
2	0.01917	0.02456	52.1648	40.7166
3	0.02232	0.02588	44.8029	38.6399
4	0.02005	0.02446	49.8753	40.8831
5	0.01988	0.02210	50.3018	45.2489
6	0.02140	0.02523	46.7290	39.6354
7	0.01822	0.02140	54.8847	46.7290
8	0.02142	0.02450	46.6853	40.8163
9	0.02606	0.02891	38.3730	34.5901

Table 4.4 shows that once again, the X axis achieves higher accuracy, which corresponds to smaller standard deviation than the Y axis for the stars with higher SNR, of approximately 1 % of a pixel for the X coordinate, while in the case of the Y coordinate, it is around 2 % of a pixel. For this method, a precision of approximately $\frac{1}{58}$ and $\frac{1}{44}$ of the size of a pixel for axes X and Y respectively, is reached. The results from different algorithms are discussed below.

4.2.1. Post-processing: Barycentric Coordinates

Later, the post-processing stage is applied to the obtained data, the results are presented in figure 4.9.

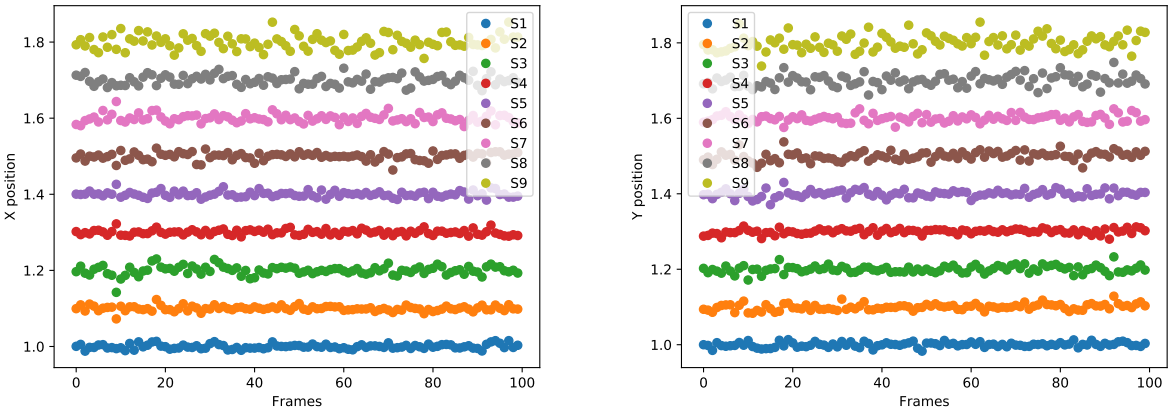

(a) Centroid of stars with Barycentric coordinates on X axis

(b) Centroid of stars with Barycentric coordinates on Y axis

Figure 4.9: Centroid of stars with Barycentric coordinates over the 100 frames

Once again, the relation between SNR and scattering is clearly present for the position of the stars, where the ones with lower SNR present more scattering than the ones with higher SNR. Also, the movement of all the stars together is corrected on both axes, as shown in figure 4.9a, and even more clearly in figure 4.9b where the remarkable slope present in the first frames is completely deleted, obtaining more stable distributions of the position of the stars.

Table 4.5: Standard deviation of the stars position calculated with Gaussian fit method and Barycentric coordinates

Star	X Standard Deviation [px]	Y Standard Deviation [px]	X Pixel Fraction [px^{-1}]	Y Pixel Fraction [px^{-1}]
1	0.00597	0.00611	167.5042	163.6661
2	0.00644	0.00808	155.2795	123.7624
3	0.01166	0.00916	85.7633	109.1703
4	0.00668	0.00659	149.7006	151.7451
5	0.00745	0.00906	134.2282	110.3753
6	0.00963	0.01157	103.8422	86.4304
7	0.01064	0.00955	93.9850	104.7120
8	0.01259	0.01527	79.4281	65.4879
9	0.01876	0.02059	53.3049	48.5673

Table 4.5 shows the standard deviation and the pixel fraction for all stars in both axes. An overall improvement on performance with respect to the previous algorithm can be remarked. It can be seen that star 1, that has higher SNR, reaches a standard deviation of approximately 0.6 % of a pixel, that corresponds to a pixel fraction of approximately $\frac{1}{165}$ of the size of a pixel, equivalent to 0.034μm. The standard deviation of all the stars it is significantly lower than the previous values obtained before the post-processing, showed in table 4.4. In addition, just as shown for the Center of gravity algorithm results, after applying the post-processing stage the accuracy values for both axes are similar in all the stars, which contrasts with the values shown in table 4.4 where the values of the standard deviation for the X coordinate were lower for most of the stars.

4.2.2. Standard Deviation through frames

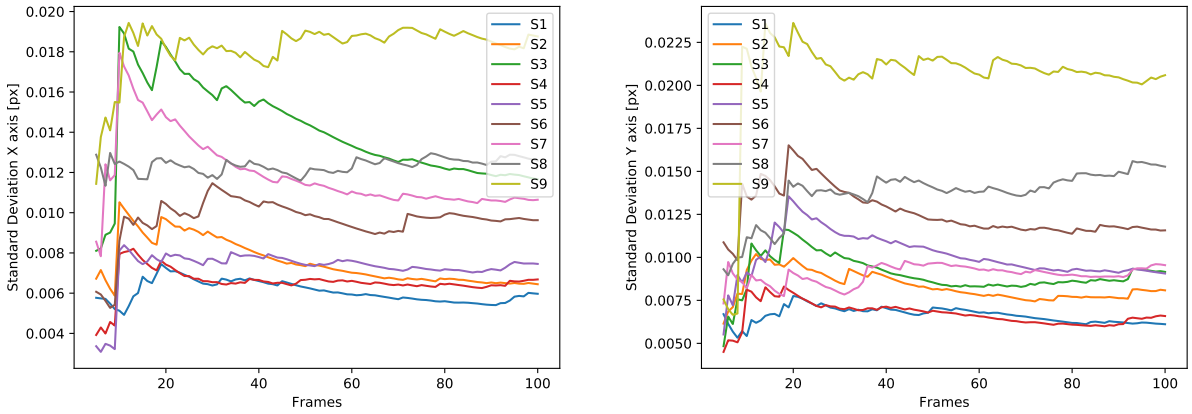

(a) Standard deviation through frames on X axis

(b) Standard deviation through frames on Y axis

Figure 4.10: Standard deviation through frames utilizing Gaussian fit method and Barycentric coordinates

Figure 4.10 shows how the standard deviation for each star changes as the amount of frames considered for the calculation increases. It can be seen that the stars with lower SNR present higher standard deviations with less stability on both axes, except for the case of star 3 that presents unusual higher standard deviation on X axis for its SNR value.

4.2.3. Standard deviation with different apertures

Finally, figure 4.11 shows the considered aperture radius versus the standard deviation calculated. It is noticed that the standard deviation for all stars on both axes stabilizes from an aperture radius of 5 pixels upwards.

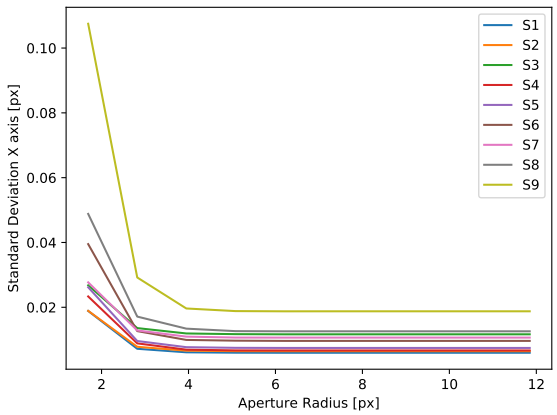

(a) Standard deviation with different apertures on X axis

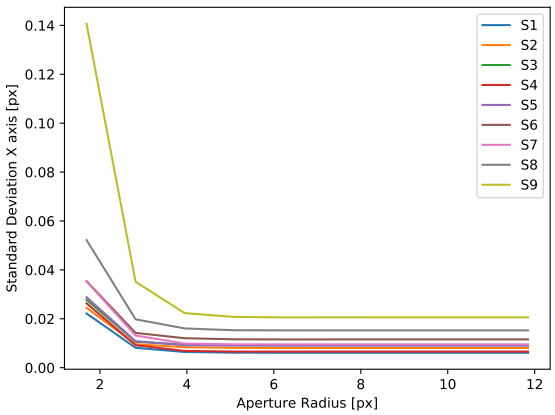

(b) Standard deviation with different apertures on Y axis

Figure 4.11: Standard deviation with different apertures utilizing Gaussian fit method and Barycentric coordinates

4.3. Fit with Airy function

The next applied image centering algorithm is the fit with an Airy function. The first results are shown in figure 4.12.

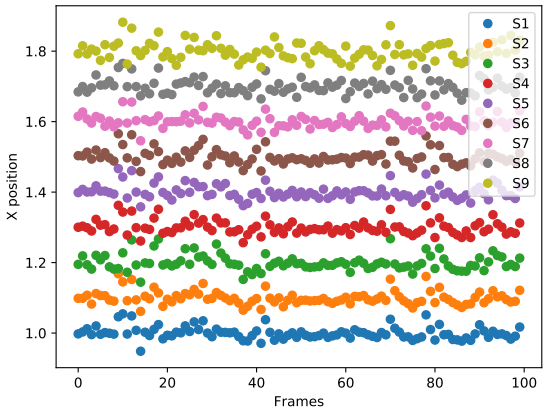

(a) Centroid of stars on X axis

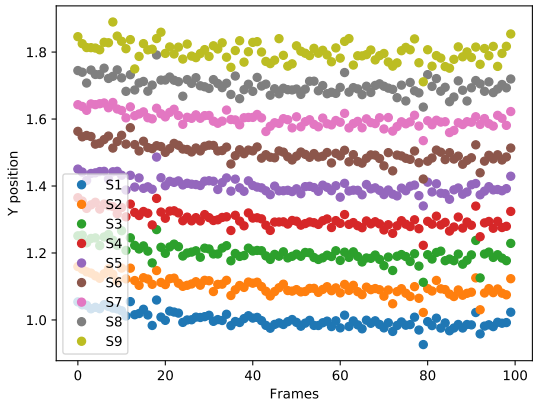

(b) Centroid of stars on Y axis

Figure 4.12: Centroid of stars over the 100 frames

Once again, small jumps of all stars can be seen on both axes, around frame 15, 40 and 80 on the X coordinate in figure 4.12a, and around frame 18, 36 and 80 on the Y coordinate in figure 4.12b. This last figure also shows the already known slope over the initial frames. The behavior shown in figure 4.12 is similar to the one obtained with the Gaussian fit method, shown in figure 4.8, and is also notable the same relation between SNR and scattering.

Table 4.6: Standard deviation of the stars position calculated with Airy function fit method

Star	X Standard Deviation [px]	Y Standard Deviation [px]	X Pixel Fraction [px^{-1}]	Y Pixel Fraction [px^{-1}]
1	0.01744	0.02262	57.3394	44.2087
2	0.01915	0.02451	52.2193	40.7997
3	0.02228	0.02579	43.8596	38.7747
4	0.02002	0.02434	49.9500	41.0846
5	0.01982	0.02206	50.4541	45.3309
6	0.02130	0.02521	46.9484	39.6668
7	0.01811	0.02121	55.2181	47.1476
8	0.02118	0.02438	47.2144	41.9172
9	0.02524	0.02821	39.6197	35.4484

Table 4.6 shows the standard deviation values and the pixel fraction values for all the stars on both axes. The results are really similar to the ones obtained with the Gaussian fit method, shown in table 4.4, reaching smaller standard deviations on the X coordinate of approximately 1 % of a pixel for the X coordinate, while in the case of the Y coordinate, it is around 2 % of a pixel. For this method, a precision of approximately $\frac{1}{57}$ and $\frac{1}{44}$ of the size of a pixel for axes X and Y respectively, is reached, which is almost identical to the precision achieved with the Gaussian fit method.

4.3.1. Post-processing: Barycentric Coordinates

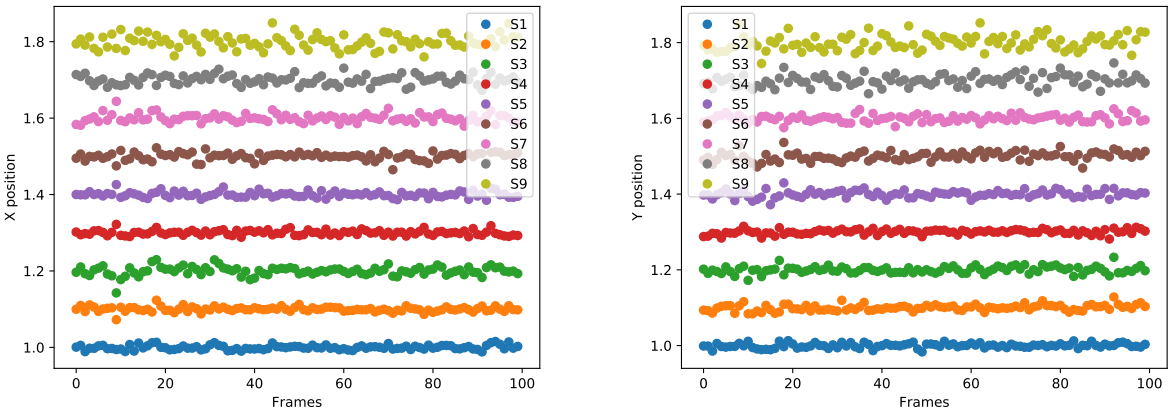

(a) Centroid of stars with Barycentric coordinates on X axis

(b) Centroid of stars with Barycentric coordinates on Y axis

Figure 4.13: Centroid of stars with Barycentric coordinates over the 100 frames

Figure 4.13 shows that after the post-processing stage, both axes have a clearly more stable behavior than in figure 4.12, maintaining the relation between SNR and scattering.

Table 4.7: Standard deviation of the stars position calculated with Airy function fit method and Barycentric coordinates

Star	X Standard Deviation [px]	Y Standard Deviation [px]	X Pixel Fraction [px^{-1}]	Y Pixel Fraction [px^{-1}]
1	0.00586	0.00595	170.6485	168.0672
2	0.00631	0.00797	158.4786	125.4705
3	0.01156	0.00896	86.5052	111.6071
4	0.00644	0.00628	155.2795	159.2357
5	0.00727	0.00879	137.5516	113.7656
6	0.00948	0.01132	105.4852	88.3392
7	0.01045	0.00907	95.6938	110.2534
8	0.01192	0.01497	83.8926	66.8003
9	0.01769	0.01963	56.5291	50.9424

Table 4.7 shows the standard deviation values and the pixel fraction values for all the stars on both axes after the application of the post-processing stage. It can be seen that star 1, that has higher SNR, reaches a standard deviation of approximately 0.59 % of a pixel, that corresponds to a pixel fraction of approximately $\frac{1}{169}$ of the size of a pixel, equivalent to 0.034μm. The standard deviation of all the stars is significantly lower than the previous values obtained before the post-processing, showed in table 4.6. Furthermore, the accuracy values for both axes are similar in all the stars, which contrasts with the values shown in table 4.6 where the values of the standard deviation for the X coordinate were lower for most of the stars.

The Airy function fit appears to provide a further small improvement on Gaussian centering, which shall be discussed below.

4.3.2. Standard Deviation through frames

Figure 4.14 shows how the standard deviation for each star found with this method changes as the amount of frames considered for the calculation increases. As the previous results, the stars with lower SNR present higher standard deviations and less stability, even in the final frames. Also, the strange behavior of star 3 for the X coordinate, shown in figure 4.10a it is seen again in figure 4.14a with unusual higher standard deviation.

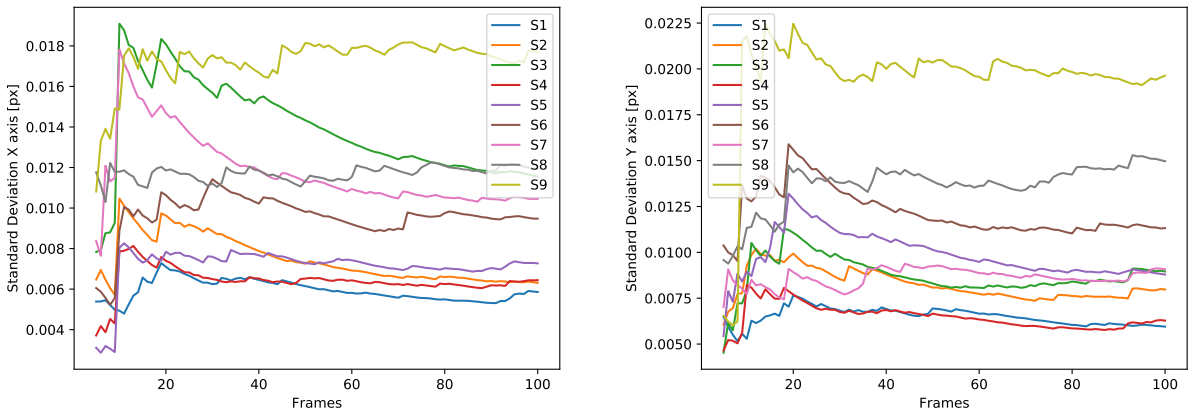

(a) Standard deviation through frames on X axis

(b) Standard deviation through frames on Y axis

Figure 4.14: Standard deviation through frames utilizing Airy fit method and Barycentric coordinates

4.3.3. Standard deviation with different apertures

Finally, the standard deviation for different aperture radius is shown in figure 4.15 where it can be seen that the standard deviation on both axes stabilizes from an aperture radius of 7 pixels upwards.

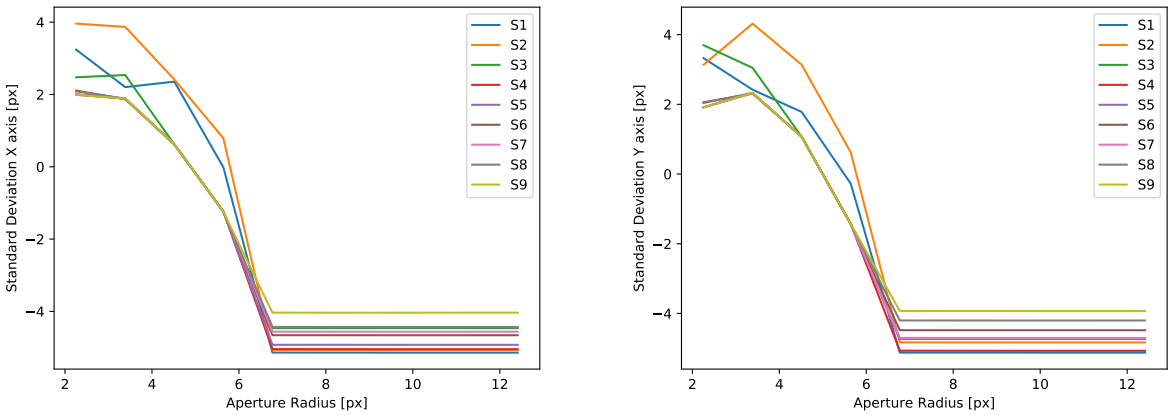

(a) Standard deviation with different apertures on X axis

(b) Standard deviation with different apertures on Y axis

Figure 4.15: Standard deviation with different apertures utilizing Airy fit method and Barycentric coordinates

4.4. Maximum Likelihood with Gaussian function as a model

Next, the image centering algorithm Maximum likelihood with a Gaussian function as a model was applied to the data. The results are shown in figure 4.16.

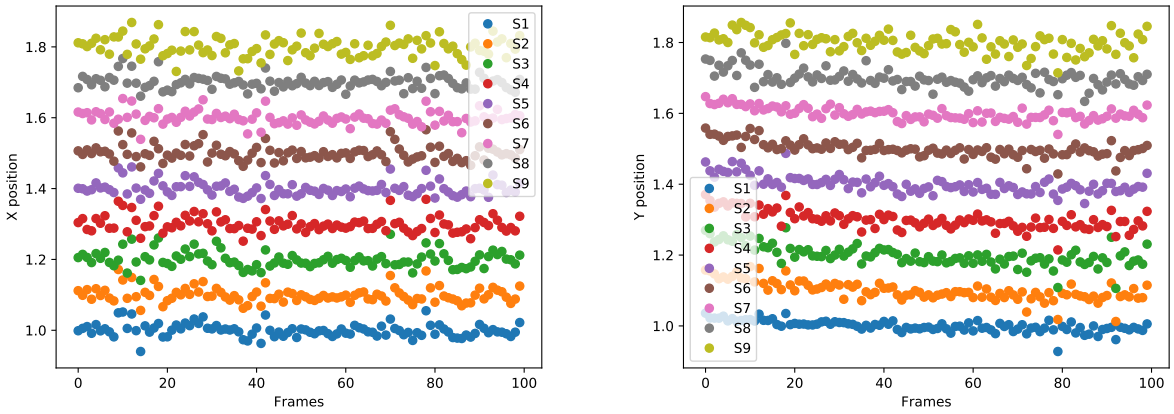

(a) Centroid of stars on X axis

(b) Centroid of stars on Y axis

Figure 4.16: Centroid of stars over the 100 frames

It is shown in figure 4.16 that the position of the centroids are roughly stable on both axes, with small jumps of all the stars around frame 15, 40 and 80 for X coordinate, as shown in figure 4.16a, while on the Y coordinate, the small jumps around frame 18 and 80 are less pronounced as shown in figure 4.16b. This figure also shows a slope on the first frames of the sample. Furthermore, it is notable the same relation between SNR and scattering as in the other methods.

Table 4.8: Standard deviation of the stars position calculated with Maximum Likelihood method with Gaussian function as a model

Star	X Standard Deviation [px]	Y Standard Deviation [px]	X Pixel Fraction [px^{-1}]	Y Pixel Fraction [px^{-1}]
1	0.01845	0.01561	55.2005	64.0615
2	0.02089	0.02683	47.8698	37.2717
3	0.02277	0.02915	43.9174	34.3053
4	0.02245	0.02628	44.5434	38.0518
5	0.01951	0.02383	51.2558	41.9639
6	0.02090	0.02158	47.8469	46.3392
7	0.01903	0.01791	52.5486	55.8347
8	0.01870	0.02478	53.4759	40.3551
9	0.02686	0.02708	37.2301	36.9276

Table 4.8 shows the standard deviation and the pixel fraction for each star. The results show that both axes reach standard deviations of approximately 1 % of a pixel, which corresponds to approximately $\frac{1}{60}$ of the size of a pixel. Furthermore, it is remarkable that the stars with intermediate values of SNR have small standard deviations with values similar to the star with higher SNR. This behavior was not found in the obtained results of previous methods.

4.4.1. Post-processing: Barycentric Coordinates

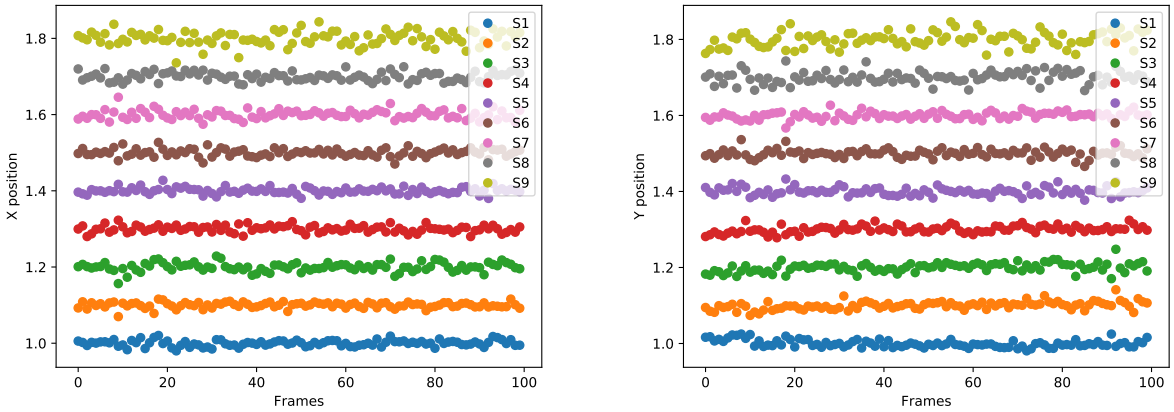

(a) Centroid of stars with Barycentric coordinates on X axis

(b) Centroid of stars with Barycentric coordinates on Y axis

Figure 4.17: Centroid of stars with Barycentric coordinates over the 100 frames

Figure 4.17 shows the results after the post-processing stage, where both axes have a clearly more stable behavior than in figure 4.16. The slope present in figure 4.16b has been completely eliminated in figure 4.17b, along with the small jumps clearly corrected, specially in figure 4.17a. Also the relation between SNR and scattering is maintained.

Table 4.9: Standard deviation of the stars position calculated with Maximum Likelihood method with Gaussian function as a model and Barycentric coordinates

Star	X Standard Deviation [px]	Y Standard Deviation [px]	X Pixel Fraction [px^{-1}]	Y Pixel Fraction [px^{-1}]
1	0.00779	0.00964	128.3697	103.7344
2	0.00730	0.01026	136.9863	97.4659
3	0.01130	0.01188	88.4956	84.1751
4	0.00870	0.00933	114.9425	107.1811
5	0.00797	0.01023	125.4705	97.7517
6	0.00973	0.01056	102.7749	94.6970
7	0.01128	0.00966	88.6525	103.5197
8	0.01119	0.01552	89.3655	64.4330
9	0.01823	0.01922	54.8546	52.0291

Table 4.9 shows the standard deviation and pixel fraction values for each star on both axes. It can be seen that star 2 reaches the higher standard deviation of approximately 0.73 % of a pixel, that corresponds to a pixel fraction of approximately $\frac{1}{137}$ of size of a pixel, equivalent to 0.041μm. In addition, it is remarkable that the stars with intermediate values of SNR, have small standard deviations comparable with star 1, that has the highest SNR. Furthermore, the pixel fraction values of the stars on the X coordinate are generally higher than the ones obtained on the Y coordinate.

The algorithm appears to evidence a mix of benefits and disadvantages, which might be further studied to ascertain e.g. the model limitations and the sensitivity to noise statistics.

4.4.2. Standard Deviation through frames

Figure 4.18 shows the change of the standard deviation for each star as the amount of frames considered for the calculation increases. It can be seen that stars with lower SNR present higher standard deviations and less stability, even in the final frames. Figure 4.18a shows that generally all the stars reach a stable value for the standard deviation in the final frames, while figure 4.18b shows that the standard deviation is still changing for some stars even in the last frames.

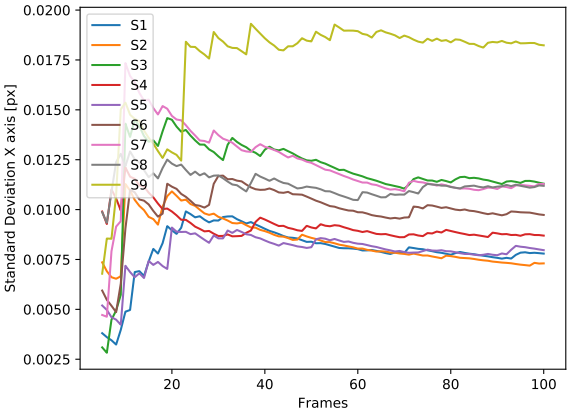

(a) Standard deviation through frames on X axis

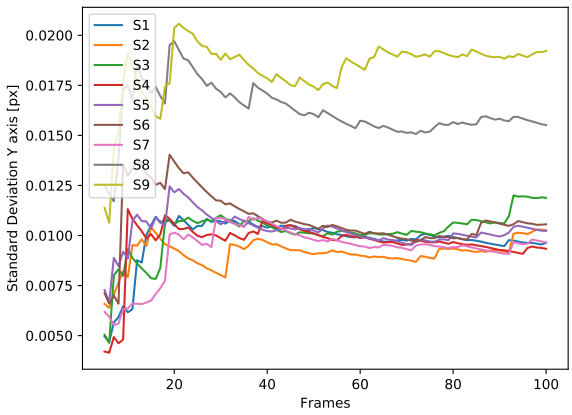

(b) Standard deviation through frames on Y axis

Figure 4.18: Standard deviation through frames utilizing Maximum likelihood method with Gaussian function as a model and Barycentric coordinates

4.4.3. Standard deviation with different apertures

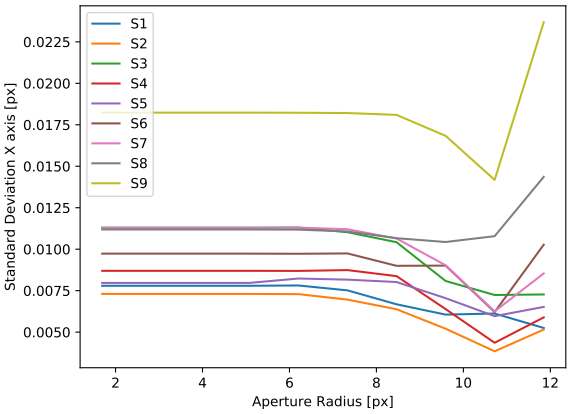

(a) Standard deviation with different apertures on X axis

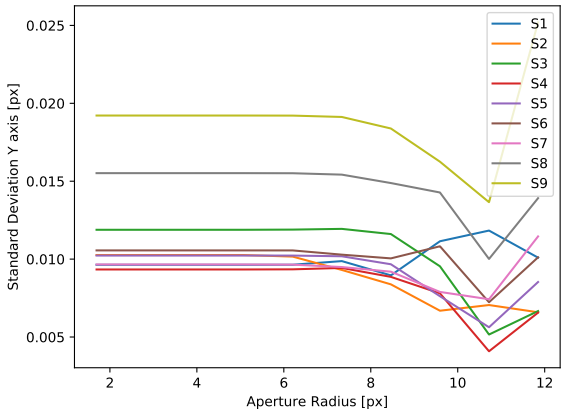

(b) Standard deviation with different apertures on Y axis

Figure 4.19: Standard deviation with different apertures utilizing Maximum likelihood method with Gaussian function as a model and Barycentric coordinates

Finally, the standard deviation for different aperture radius is shown in figure 4.19 where it can be seen that the standard deviation on both axes shows an optimal value for the aperture where the standard deviation is maximized, around 11 pixels.

4.5. Maximum Likelihood with Airy function as a model

The final image centering algorithm applied to the data was the maximum likelihood but this time with an Airy function as a model.

The obtained results were scaled utilizing a scaling factor due to an unusual behavior of variables. This scaling factor was obtained finding the mean of the pixel fraction on both axes for star 9, that has the lower SNR. Later, the relation between the Cramér-Rao astrometric limit and this value was found. The resulting value is 0.1823 and corresponds to the mentioned scaling factor. All the found values for the post-processing with this method were multiplied for this scaling factor, obtaining the values shown in table 4.10.

Table 4.10: Standard deviation of the stars position calculated with Maximum Likelihood method with Airy function as a model and Barycentric coordinates

Stars	X Standard Deviation [px]	Y Standard Deviation [px]	X Pixel Fraction [px^{-1}]	Y Pixel Fraction [px^{-1}]
1	0.01391	0.00744	71.8776	134.3289
2	0.00827	0.00912	120.9341	109.6752
3	0.01140	0.00837	87.6715	119.4586
4	0.00681	0.00560	146.8940	178.5139
5	0.00820	0.00632	121.9315	158.1315
6	0.00694	0.00985	144.0104	101.5743
7	0.00782	0.00750	127.8840	133.2835
8	0.00815	0.01085	122.7176	92.1612
9	0.01744	0.01549	57.3186	64.5508

Table 4.10 shows the standard deviation and the pixel fraction for all stars on both axes. It can be seen that star 1 reaches a standard deviation of approximately 0.7 % of a pixel, that corresponds to a pixel fraction of approximately $\frac{1}{128}$ of the size of a pixel, equivalent to 0.044μm, which is the highest for all stars. Also, just as the values shown in table 4.9, the stars with intermediate values of SNR, present higher values for the pixel fraction, comparable with the brighter star. Furthermore, the values obtained on the Y coordinate correspond, in general, to higher accuracy than the results on the X coordinate.

Some of the peculiarities of the previous case (Maximum Likelihood method with Gaussian function as a model) are confirmed.

4.6. Marginal Graphics

Another important stage of the data analysis is the study of the shape of the PSF. For this purpose, the marginal graphics were made, where the intensity value of all the pixels of each column or each row of the ROI are added, then, a function is adjusted over the obtained profile.

First, the intensity values over each column were added and graphed over the X coordinate, then a Gaussian function was adjusted over the obtained profile. This process was made for all the stars and the results are shown in figure 4.20.

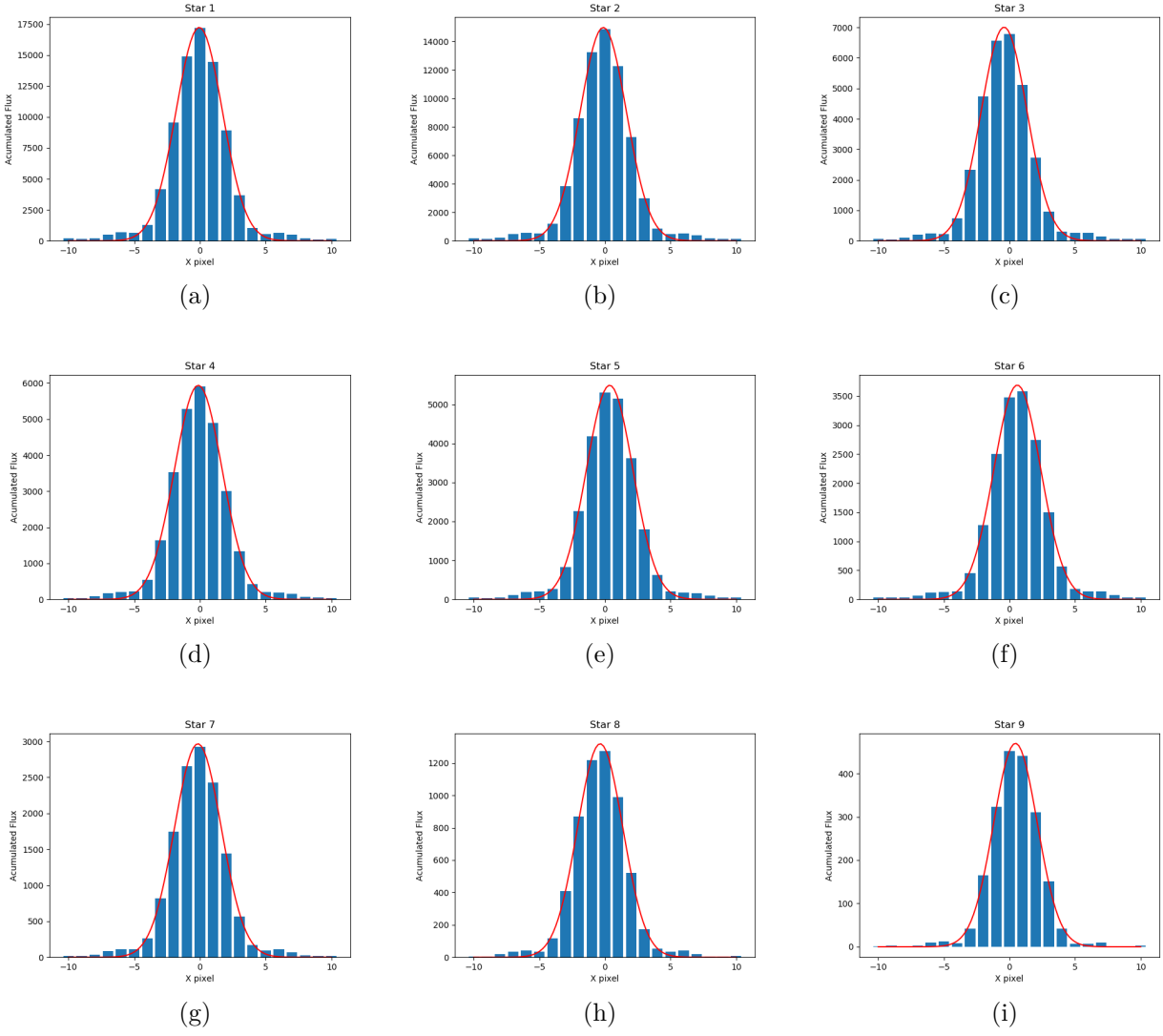

(a) (b) (c)

(d) (e) (f)

(g) (h) (i)

Figure 4.20: Marginal graphics over X coordinate with Gaussian fit

Later, the intensity values over each row were added and graphed over the Y coordinate, then a Gaussian function was adjusted over the obtained profile. This process was made for all the stars and the results are shown in figure 4.21.

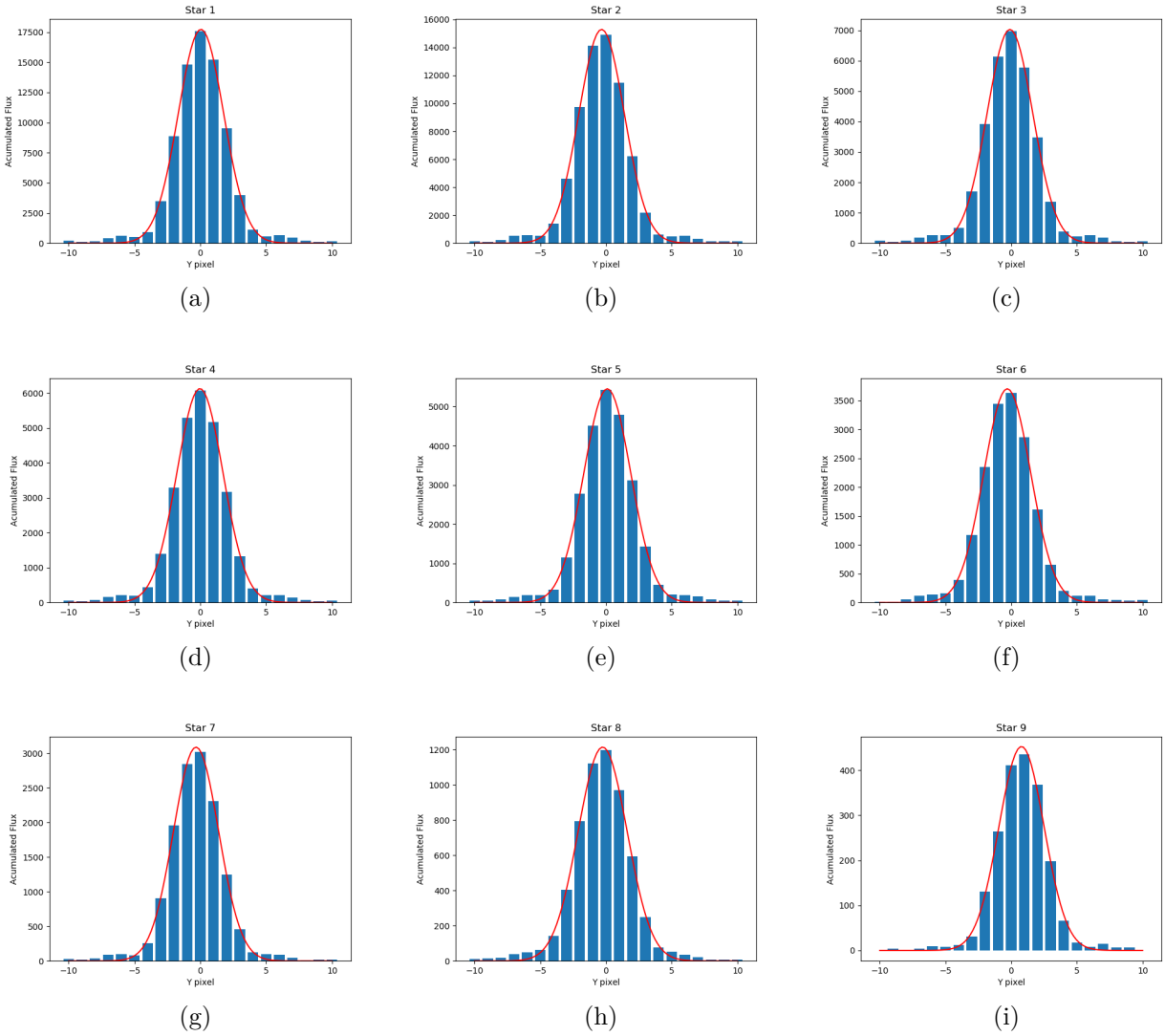

Figure 4.21: Marginal graphics over Y coordinate with Gaussian fit

Figure 4.20 and figure 4.21 show the obtained profile and the fitted Gaussian function. It can be seen that in general the Gaussian function makes a correct fit over the profile of each star, specially over the central pixel where the maximum intensity values are found, but fails to include the small intensity values of the outer pixels. Nevertheless, these figures show that the Gaussian function is a good model for the PSF of the stars with particular respect to the central peak of the light distribution.

Next, the same process was applied, but this time utilizing the Airy function as a model for the profile data, as way to include the outer intensity values, that corresponded to the observed diffraction rings.

The intensity values over each column were added and graphed over the X coordinate, then, an Airy function was adjusted over the obtained profile. The results are shown in figure 4.22.

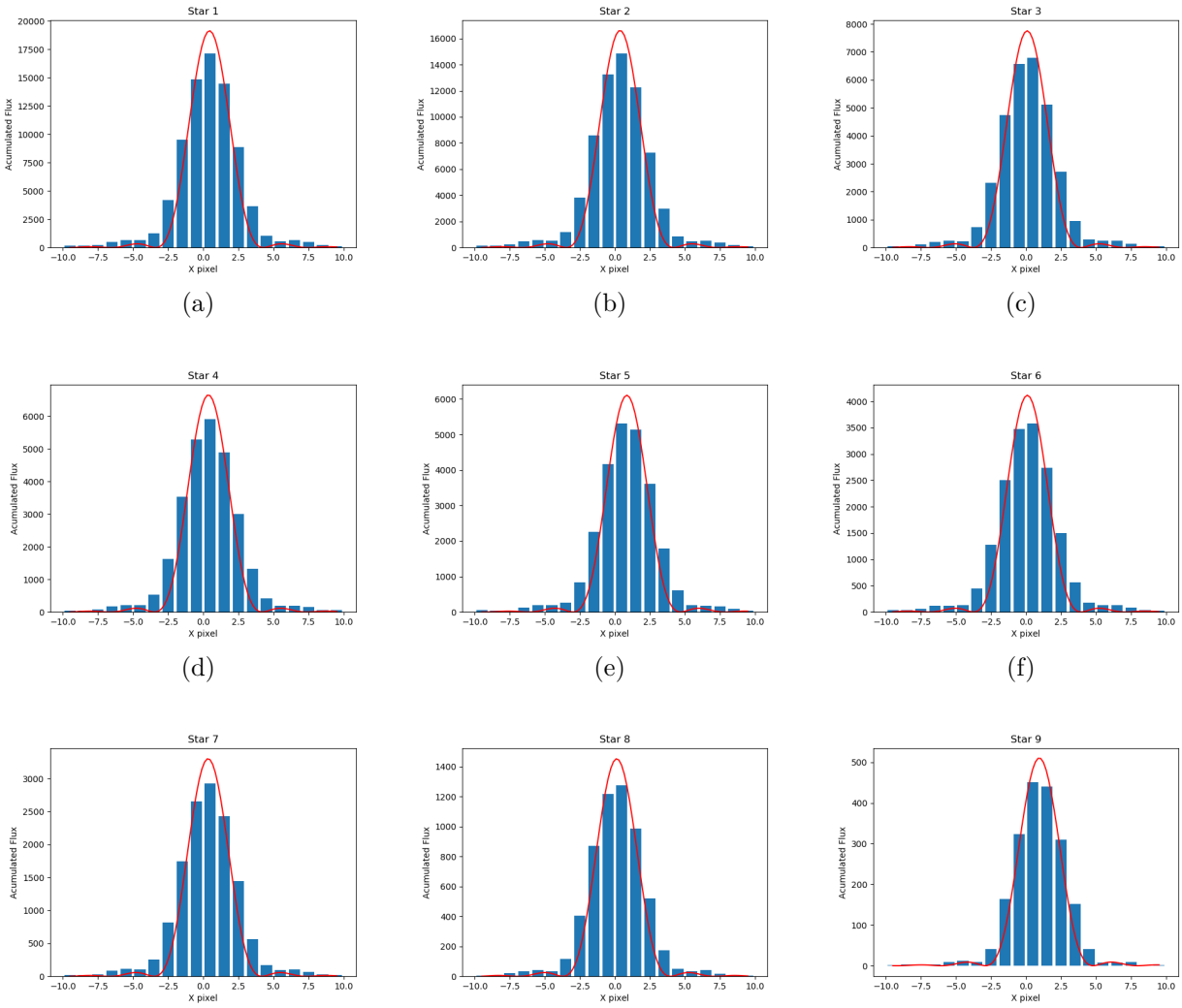

(a) (b) (c)

(d) (e) (f)

(g) (h) (i)

Figure 4.22: Marginal graphics over X coordinate with Airy function fit

Finally, the intensity values over each row were added and graphed over the Y coordinate, then an Airy function was adjusted over the obtained profile. This process was made for all the stars and the results are shown in figure 4.23.

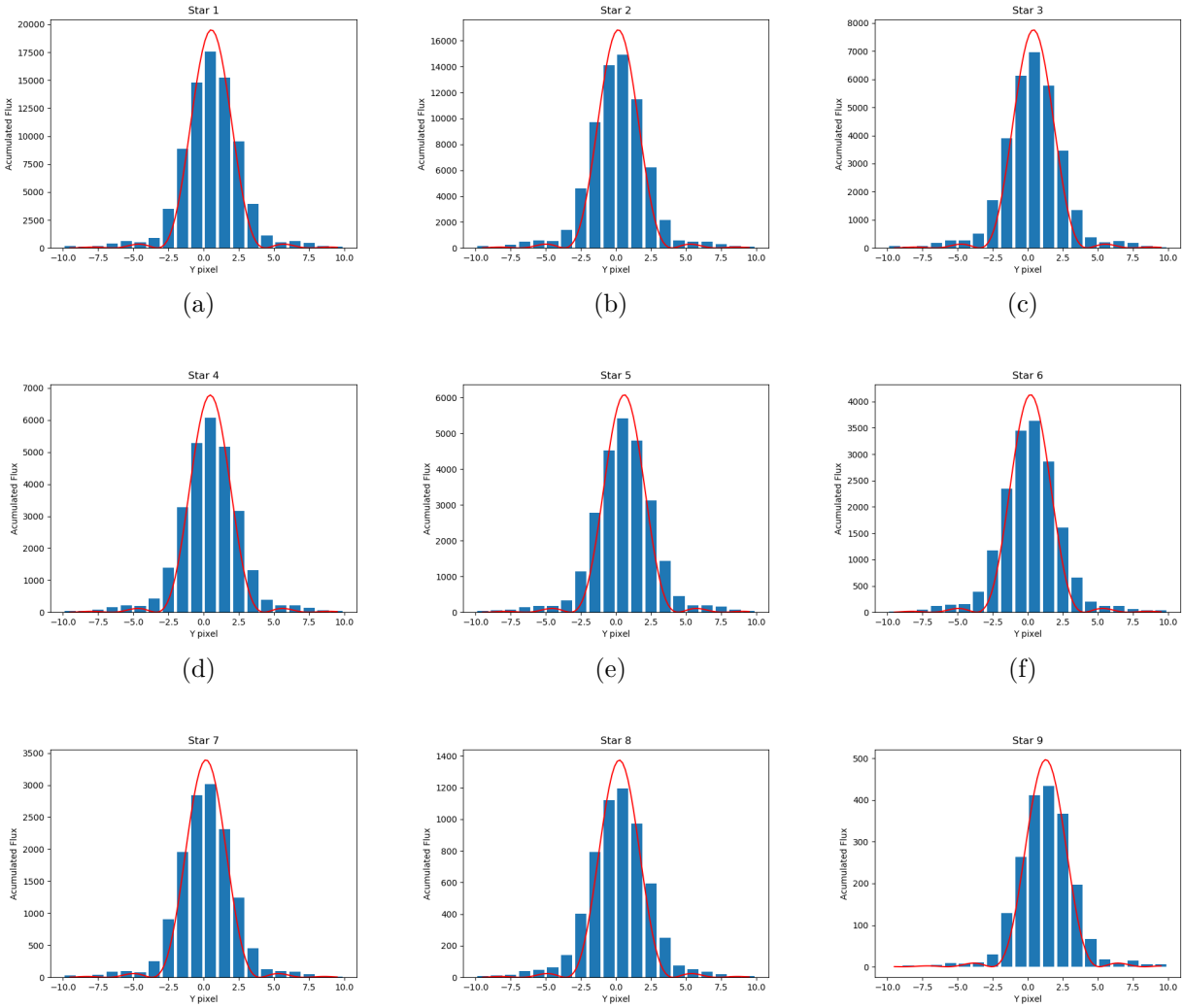

Figure 4.23: Marginal graphics over Y coordinate with Airy function fit

Figure 4.22 and figure 4.23 show the obtained profile and the fitted Airy function. It can be seen that the Airy function properly adjust the profile in the outer pixels, but fails to adjust the maximum value over the central pixel. However, the Airy function shows that is a good approximate model for the PSF of these stars in the peripheral region. It appears that a more complex model may be required to achieve a better fit to our data. The issue may be verified in future runs of the experiment.

4.7. Differences between methods using Gaussian fit as comparison

The next step was to study the difference between the calculated position of the centroid on each axis in each frame for one of the methods and the Gaussian fit.

Figure 4.24 shows the difference between the Gaussian fit method and the Center of Gravity algorithm versus the position of the pixel on each axis. The black dots show a $\pm\sigma$ from the average on each star.

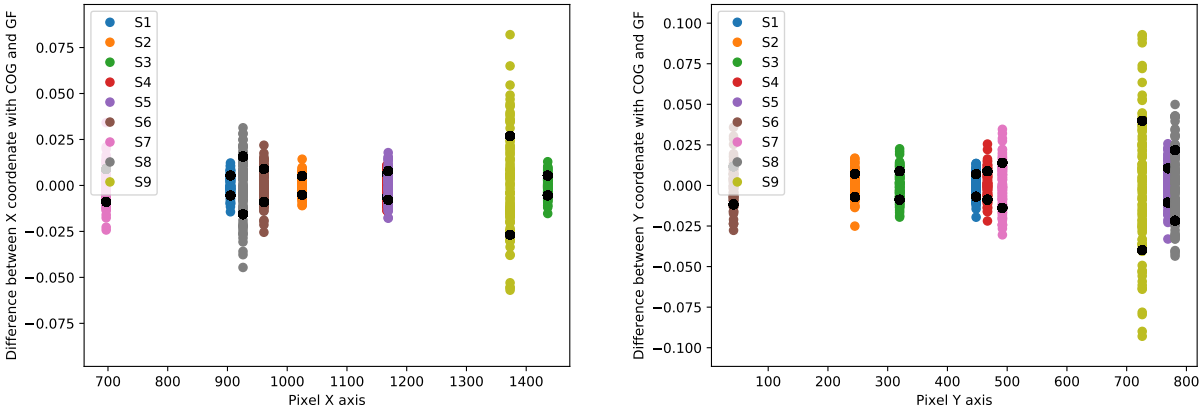

(a) Difference between Gaussian fit and Center on gravity method on X axis

(b) Difference between Gaussian fit and Center on gravity method on Y axis

Figure 4.24: Difference between Gaussian fit and Center on gravity method

Figure 4.25 shows the difference between the Gaussian fit method and the Maximum likelihood algorithm with a Gaussian function as model versus the position of the pixel on each axis. The black dots show a $\pm\sigma$ from the average on each star.

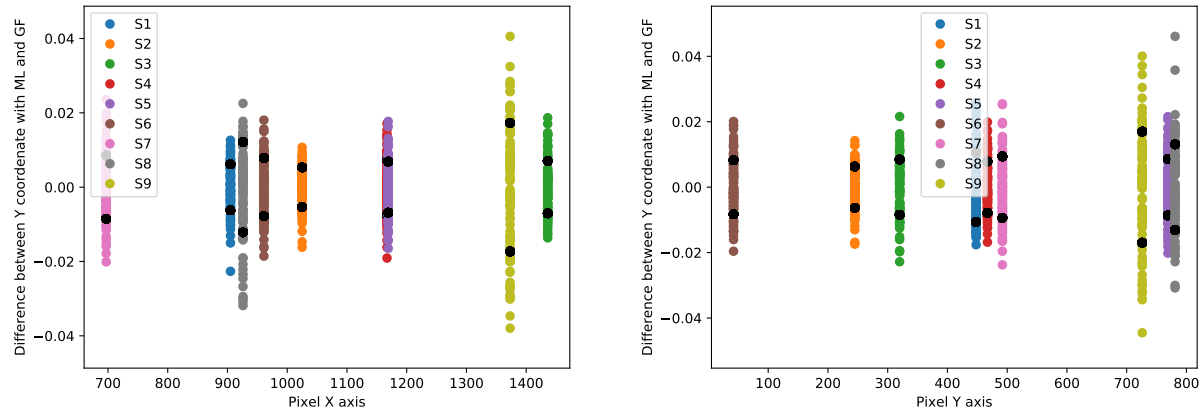

(a) Difference between Gaussian fit and Maximum Likelihood with Gaussian function as a model on X axis

(b) Difference between Gaussian fit and Maximum Likelihood with Gaussian function as a model on Y axis

Figure 4.25: Difference between Gaussian fit and Maximum Likelihood with Gaussian function as a model

Finally, figure 4.26 shows the difference between the Gaussian fit method and the fit with an Airy function algorithm versus the position of the pixel on each axis. The black dots show a $\pm\sigma$ from the average on each star.

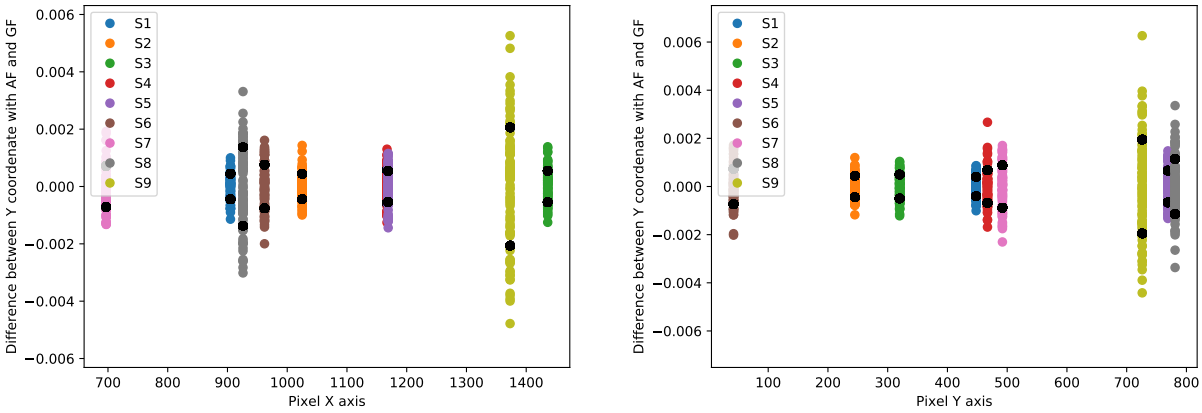

(a) Difference between Gaussian fit and Fit with Airy function on X axis

(b) Difference between Gaussian fit and Fit with Airy function on Y axis

Figure 4.26: Difference between Gaussian fit and Fit with Airy function

These figures show that the star with lower SNR has the highest dispersion on both axes, followed for star 8, the second star with lower SNR. On the other hand, the stars with higher SNR have the smallest dispersion.

Another remarkable feature is that figure 4.24 and 4.26, in general, have considerable smaller differences than the ones presented in figure 4.25.

4.8. Performance achieved with different methods

To summarize the performance of the applied image centering algorithms, the pixel fraction values on each star for each method were graphed. The results are shown in figure 4.27.

Figure 4.27a shows the performance of the image centering algorithms in the X coordinate, where it is possible to notice that all the algorithms, with the exception of the Maximum Likelihood with an Airy function as a model, have a similar behavior. The Center of gravity algorithm has the worst operation at stars with lower SNR, while in stars with higher SNR the Maximum likelihood algorithms have the most inferior performance, where the approximate limit between the two previously described behaviors is star 3. In that point all the image centering algorithms have the same performance, that is remarkable low in comparison with the adjacent stars. Also, it is possible to notice that the Gaussian fit and the Airy fit have the same behavior for all stars, but the latter is in general slightly better, nevertheless, both algorithms have the best performance for stars with higher SNR, while for stars with

lower SNR, that role is played by the Maximum likelihood methods.

Part of the explanation may relate to the discrepancy between either model and our data (Sec. 4.6), and better efficiency of Maximum Likelihood methods in rejecting noise from peripheral regions.

Figure 4.27b shows the performance of the image centering algorithms in the Y coordinate, where all the algorithms have a similar behavior. Like figure 4.27a, the Center of gravity method has the worst performance for lower SNR, while for higher SNR it is the Maximum likelihood methods. Also, for higher SNR the Airy and Gaussian fit have the best operation while for lower SNR, the Maximum Likelihood methods work better. Furthermore, on Y axis, the different algorithms do not achieve the same values for star 3, and despite presenting a small decay in efficiency, it is much smaller than in figure 4.27a.

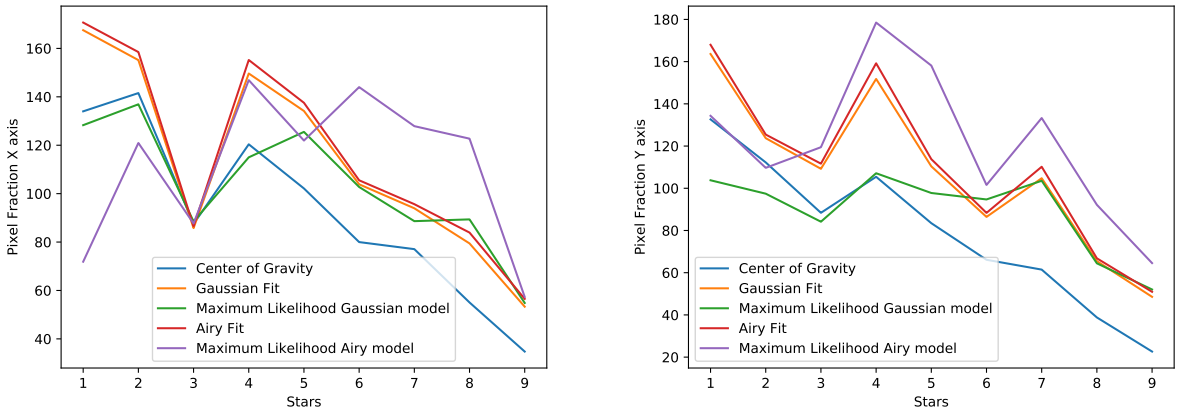

(a) Pixel fraction of stars with different methods on X axis

(b) Pixel fraction of stars with different methods on Y axis

Figure 4.27: Pixel fraction of stars with different methods

4.9. Cramér-Rao Limit

Once all the image centering algorithms have been applied, the Cramér-Rao astrometric limit was calculated utilizing equation 2.15 on the regime where the flux dominates over background due to the characteristics of the data. For this purpose, the FWHM and the flux were calculated as described earlier for the SNR computation, while the utilized gain value was the one detailed on Chapter 3, of $7.324e^{-}$/ADU.

Table 4.11 shows the Cramér-Rao astrometric limit values for all stars, as well as the Cramér-Rao standard deviation, that corresponds to the square root of the calculated limit. Finally, it is shown the Cramér-Rao pixel fraction that is the reciprocal of the standard deviation, for a better visualization of the results. It is possible to notice that the SNR and the Cramér-Rao astrometric limit have a indirect relation, i.e. for higher SNR, the Cramér-Rao

astrometric limit has smaller values. The same occurs with the Cramér-Rao standard deviation.

Table 4.11: Cramér-Rao astrometric limit

Star	Cramér-Rao Astrometric Limit [px^2]	Cramér-Rao Standard Deviation [px]	Cramér-Rao Pixel Fraction [px^{-1}]
1	$6.7248 \cdot 10^{-6}$	0.002593	385.6218
2	$7.7571 \cdot 10^{-6}$	0.002785	359.0461
3	$1.6764 \cdot 10^{-5}$	0.004094	244.2349
4	$1.9137 \cdot 10^{-5}$	0.004375	228.5926
5	$2.1091 \cdot 10^{-5}$	0.004593	217.7461
6	$3.1053 \cdot 10^{-5}$	0.005572	179.4532
7	$3.9020 \cdot 10^{-5}$	0.006247	160.0871
8	$9.1344 \cdot 10^{-5}$	0.009557	104.6306
9	$2.6940 \cdot 10^{-4}$	0.01641	60.9249

4.10. Performance comparison of tested algorithms against Cramér-Rao limit

Finally, the Cramér-Rao astrometric limit was compared with the results obtained from all the image centering algorithms applied to the data. For this purpose, the Cramér-Rao pixel fraction was graphed with the pixel fraction values obtained utilizing the centering methods for each star. The results are shown in figure 4.28.

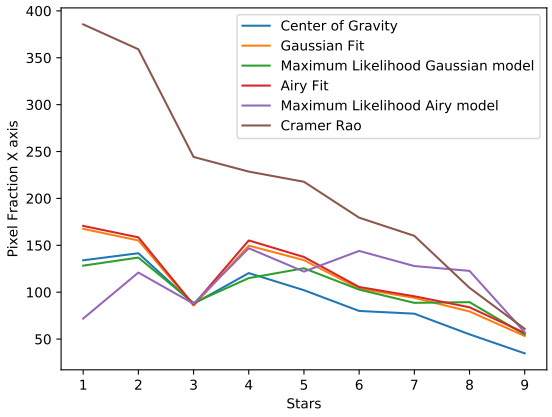

(a) Pixel fraction of stars with different methods and Cramér-Rao limit on X axis

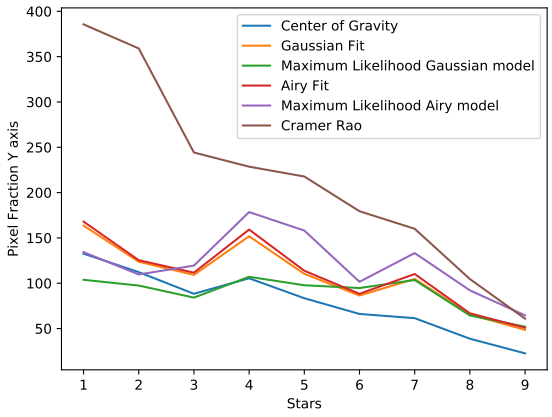

(b) Pixel fraction of stars with different methods and Cramér-Rao limit on Y axis

Figure 4.28: Pixel fraction of stars with different methods and Cramér-Rao limit

Figure 4.28 shows the same results as figure 4.27 but including the pixel fraction of the Cramér-Rao astrometric limit. It is possible to notice that on both axes, for the star with lower SNR, the image centering algorithms, with the exception of the Center of gravity method, have a performance close to the Cramér-Rao limit. Besides, the curve of the Cramér-Rao limit separates more and more from the curves of the behavior of the algorithms as the SNR of the considered stars increases. The discrepancy increases steadily for increasing SNR, e.g. from star 4 to brighter cases.

In addition, figure 4.28a shows that the Cramér-Rao limit is exceeded at star 8 for the Maximum likelihood algorithm with an Airy function as a model by a small amount. This may be ascribed to the uncertainty on parameters, and the limited size of the statistical sample.

After obtaining this figure that compares the achievable experimental accuracy with different methods and the astrometric Cramér-Rao limit, the results of this work are complete.

Chapter 5

Discussion

After reviewing the results, it is necessary to move on to the next stage of this work, which corresponds to the discussion of these obtained results and of various aspects of the methodology.

5.1. Discussion about the methods

As explained in Chapter 3, the experimental process, from the design of the experiment until the results were obtained, corresponded to an iterative procedure, where in each iteration the quality of the experiment was enhanced, which led to an improvement of the obtained results. In order to obtain the data studied in this work, it was necessary to perform several iterations of the optical alignment and the data collection, as shown in figure 3.1.

The first obtained data set was a functional test, i.e. a data collection with the purpose of verify that the setup was functioning correctly, well aligned and with focused image. A second functional test was performed with the same purpose, after moving the location of the experimental setup to a clean dark room. A third measurement was made with the detector rotated by 180 degrees to study the behavior of the Y coordinate in a stabilized environment. Due to the poor sampling of the central peak in the point-like sources, a fourth data set was obtained adjusting the optics to have defocused stars, having more pixels in the central peak, nevertheless, the defocus was too much, providing excessively degraded images. Finally, a fifth data set was obtained closing the aperture of the detector to the minimum size, about 1 mm, achieving dispersion corresponding to larger pixel fractions on larger images. This is the data studied during work.

After all these tests, where the optical alignment was modified and improved, it was possible to obtain a data set that allowed to correctly study the maximum achievable accuracy of the position of the stars. This process required a detailed characterization of the used components, especially the bidimensional digital detector, where it was necessary to fully understand its functioning and its operating software.

This period where the experimental setup was improved and a correct configuration was found, required multiple tests as indicated above, which caused it to extend for approximately two months. The greatest complexity corresponded to the fact that at each stage new,

previously unknown experimental problems were detected and had to be studied and fixed to begin a new iteration.

This stage led to a better understanding of the relevant aspects of the experimental setup, so a few suggestions can be made to enhance future experiments. First of all, it would be better if the stars were located in the middle of the image produced by the detector, as a way to minimize the aberrations provoked by the edges of the optics. Also, it would be necessary to take more realizations of the experiments, i.e. add more frames to the measurements, as a way to stabilize the standard deviation for all stars, even the ones with low SNR regime. Furthermore, a pinhole array with smaller holes as a means to produce artificial stars with lower SNR with the goal to study the other regime of the Cramér-Rao bound, where the background dominates over flux. In addition, it would be convenient to change the light source from the experimental setup to one that emits light at the wavelength where the bi-dimensional digital detector achieves higher quantum efficiency. Some of the suggestions can be implemented also on the current setup, e.g. increasing the data sample, whereas hardware upgrades have different levels of cost and difficulty. In particular, alternative light sources are commercially available, whereas the pinhole array is custom made and cannot be easily replaced.

Later, the processing and post-processing stage began. This period had a big variability in the time required for each method, since the difficulty in its implementation depended on multiple factors. In addition, with the analysis of each method, it was necessary to perform multiple tests to ensure its correct implementation, together with subsequent analyzes that would allow a more exhaustive understanding of the obtained data. The main challenge of this stage was the detailed coding and the analysis of the utilized algorithms, where the use of Python and its tools, specially applied for the development of astronomical analyzes, were required. The produced code is robust and may be used for analysis of new data sets, as well as basis for further development. It may be noted that it is a specialized product, not suited to general purpose, and as such it is not planned to be delivered to the public.

Finally, the extensive study of the obtained results required a detailed knowledge of all the involved factors, both the experimental measurements and the coding of the image centering algorithms, to obtain the conclusions of this work.

5.2. Discussion about the results

From figure 4.2 it can be seen that indeed the point-like sources, called stars for simplicity during this work, were well sampled and focused. Also, from figure 4.3 it can be seen the appearance of the diffraction pattern due to the the dispersion of the light through the optical setup, which also confirms that the point-like sources were well focused.

Table 4.1 shows the values for the SNR and the maximum pixel value for each star. From this and its calculation it can be seen that all the star were in the regime where the flux dominates over background. This dominance is very strong for all the stars even for the ones with lower SNR. However, the distribution of intensity over about one decade allows simultaneous measurement over a significant range.

Another important analysis performed during this work was the examination of the marginal graphics, which allows to approximately study the shape of the PSF. This point was a key factor for the correct study of the maximum achievable accuracy on the determination of the position of the artificial stars, due to the dependence that the diverse image centering algorithms have on this feature. Figures 4.20 and 4.21 show that a Gaussian function is a good approximate model for the PSF shape of the artificial stars, but fails to include the intensity values of the outer pixels, which can provoke slight movements of the position of the centroid. On the other hand, figures 4.22 and 4.23 show that an Airy function also works as a model for the shape of the PSF of the artificial stars. In this case, the intensity values of the outer pixels are included but the center values are poorly fitted. This also can cause the appearance of some errors in the determination of the position of the centroid in each frame. Nevertheless, these figures verify that both functions, Gaussian and Airy, work as a good model approximation for the shape of the PSF. This confirms that the application of the fitting method with both functions, or the Maximum Likelihood method with both functions as a model, are relevant analysis. Besides, this also suggests that future work may be devoted to the development of better PSF models, providing adequate fitting over the whole range. This may further improve on the location error, specifically on both random and systematic components.

Figures 4.24, 4.25 and 4.26 show that there is not an unexpected difference among the results obtained from different methods. This appears to be an indication of adequate understanding of the experimental setup, and of robustness of the data analysis methodology and results.

Figure 4.28 requires the most extensive analysis, because corresponds to the main objective of this work, the comparison between the theoretical Cramér-Rao astrometric limit and the achievable precision of the determination of position on experimental data. In this figure it is possible to see the performance of all the different image centering algorithms applied to the obtained data and the pixel fraction of the Cramér-Rao astrometric limit. On both axes, the Maximum likelihood methods have a better performance for stars with lower SNR, while for stars with higher SNR, the Gaussian and Airy fit play this role. On the other hand, again on both axes, the Center of gravity algorithm has the worst performance for stars with lower SNR, while for stars with higher SNR, this occurs for the Maximum likelihood methods. Also it is possible to see that the curve of the Cramér-Rao limit separates more and more from the curves of the behavior of the algorithms as the SNR of the considered stars increases. Among the potential causes of this peculiarity, we must take into account the usage of barycentric coordinates: the differential technique is efficient in removing common mode disturbances, but it has the drawback of 'dumping' additional noise on the residuals, which is particularly evident on the brightest sources. Moreover, as described above, the image profile model is not yet optimal, which may impact more heavily the high SNR cases in which better performance is expected.

From the previous observations we have a lot of elements that require further analysis. First, the Center of gravity method it is the simpler algorithm utilized during this study, so as expected, our results show that it has in general a poor performance, specially for lower SNR, where other methods reach optimal behavior.

The Gaussian fit and Airy fit methods present a very similar performance on both axes for all stars. The discrepancies between the results of these methods are very small and can fall into the uncertainty associated with the performance analysis. These results also confirm that both functions are suitable models for the shape of the PSF, due to the high accuracy achievable, specially for the high SNR regime.

Finally, the Maximum likelihood method utilizing both functions, Gaussian and Airy as a model, have a great performance, close to the Cramér-Rao astrometric limit for low SNR regime, being superior to all the other methods, while for high SNR regime, present a poor performance. In spite of the results from Espinoza et al. [2018] [17], which showed that the Maximum likelihood method achieves optimal performance across a wide range of conditions, this study found that this is only true for low SNR regime, while for high SNR regime, the results are poor and far from optimality. This behavior was earlier registered, so our results are in good agreement with previous findings. [18]

The performance of the utilized algorithms is significantly poorer than the Cramér–Rao bound for the high SNR regime. On the other hand, for low SNR regime, like star 9, the algorithms evidence near optimal performance approaching to the Cramér–Rao bound. This is in line with the results found by Lobos et al. [2015] and Bouquillon et al. [2017] [19, 18], and its verification it is a really important feature of this work. This big discrepancy between the performance of the algorithms and the Cramér-Rao astrometric bound, specially for high SNR regime, needs to be interpreted with caution, and could have several possible explanations, yet two are the most satisfactory. First, these differences can be justified by the lack of development of the applied algorithms and the absence of optimization in their performance for high SNR regime. Another possible explanation it is that the Cramér-Rao astrometric bound is an ideal quantity calculated considering a gaussian PSF and other ideal assumptions, so different conditions can alter its performance. Also, the electro-optical response of the pixel array, and its variation over the detector, is described as mostly ideal. In other words, the Cramér-Rao limit has been derived in an exceedingly simplified model of the experimental system, thus providing overly optimistic results. This error sources add uncertainty that could move down the Cramér-Rao bound curve, approaching it to the performance of the applied methods. This two possible explanations require further studies that are suggested as future work.

Another relevant discussion is the behavior of star 3 on the X coordinate, that presents a remarkable low performance in comparison with the stars with similar SNR regime. The reason for this rather contradictory result is not completely clear but it can be attributed to the position of star 3 on the X coordinate of the image produced by the detector (Fig. 4.1). This star is located further to the right in the image, followed by star 9. This unexpected results can be explained by possible optical aberrations on the outer regions of the image produced, for example, by the edges of the lens or other optical components. Although, this cannot be confirmed by the results obtained for star 9, because it has a low SNR regime, completely different from the case of star 3. Despite the limitations of this star, it can be treated as an isolated situation, so the obtained results can be neglected for rest of the data analysis.

Next, it is necessary to mention the performance of the Maximum likelihood with an Airy function as a model where it was necessary to include a scaling factor to mitigate unrealistic results. Despite the limitations of this method, and consequently its poor results, our findings suggest that the introduction of the scaling factor partially fixes the unexpected observations.

Finally, there is evidence to suggest that we experimentally verified the limit behavior of the Cramér-Rao astrometric bound, since the performance of all the applied methods was sub-optimal, and none of them surpasses the theoretical value for the standard deviation of the position of the stars by significant amounts.

Chapter 6

Conclusion

During this work, we have devised a methodology that managed to design and implement an experimental setup that allowed accurate astrometric measurements with a bidimensional digital detector. The obtained data was analyzed applying different image centering algorithms which made possible the analysis of its performances and the calculation of the astrometric Cramér-Rao limit.

Despite the limitation of one of the studied methods, in general, we obtained accurate data that allowed us to corroborate previous researches, like the results obtained by Lobos et al. [2015] [19] and also, provide further evidence of the performance of different image centering algorithms.

Our research has made considerable progress in the study of the maximum achievable accuracy for the determination of the position of a star and its relation with Cramér-Rao astrometric bound. In conclusion, our work achieves the main objective consisting in the verification of the limit behavior of the Cramér-Rao bound for the maximum reachable location precision, and also led to a better understanding of the relevant aspects of the experimental setup. The candidate's activity mainly focused on data reduction and analysis, but significant contributions were provided on experimental setup operation and iterative optimization.

These observations have several implications for research into the characterization of bidimensional digital detectors and the achievement of higher accuracy on astrometric measurements. Also, our techniques could be applied to the design of astrometric space missions and satellites to further improve the observations. Furthermore, this was applied to the ASTRA project, a bilateral cooperation between China and Italy with the goal of consolidating astrometric measurement concepts and technologies.[20]

Further work needs to be performed to establish whether the relevant discrepancy between the Cramér-Rao limit and the performance of the applied image centering algorithms is due to the ideal conditions utilized to derive the Cramér-Rao theoretical bound (model limitations) or if it is due to the poor performance of the applied centering algorithms (implementation issues). Furthermore, future tests should apply the recommended improvements for the experimental setup, some of which are in progress, in order to achieve higher precision with better astrometric measurements. As shown, this work establishes itself as a precedent for future research.

Bibliography

[1] R. A. Mendez, J. F. Silva, and R. Lobos, "Analysis and interpretation of the cramér-rao lower-bound in astrometry: One-dimensional case," *Publications of the Astronomical Society of the Pacific*, vol. 125, no. 927, p. 580, 2013.

[2] R. A. Mendez, J. F. Silva, R. Orostica, and R. Lobos, "Analysis of the cramér-rao bound in the joint estimation of astrometry and photometry," *Publications of the Astronomical Society of the Pacific*, vol. 126, no. 942, p. 798, 2014.

[3] J. Janesick and M. Blouke, "Sky on a Chip: The Fabulous CCD," , vol. 74, p. 238, Sept. 1987.

[4] I. S. McLean, *Electronic Imaging in Astronomy: Detectors and Instrumentation (Second Edition)*. 2008.

[5] S. B. Howell, *Handbook of CCD Astronomy*, vol. 5. 2006.

[6] A. Hoffman, M. Loose, and V. Suntharalingam, "Cmos detector technology," *Experimental Astronomy*, vol. 19, no. 1-3, pp. 111–134, 2005.

[7] B. Burke, P. Jorden, and P. Vu, "Ccd technology," *Experimental Astronomy*, vol. 19, no. 1-3, pp. 69–102, 2005.

[8] H. Karttunen, P. Kröger, H. Oja, M. Poutanen, and K. J. Donner, *Fundamental Astronomy*. Springer Science & Business Media, 2007.

[9] W. J. Merline and S. B. Howell, "A Realistic Model for Point-sources Imaged on Array Detectors: The Model and Initial Results," *Experimental Astronomy*, vol. 6, pp. 163–210, Jan. 1995.

[10] M. Gai, D. Carollo, M. Delbò, M. Lattanzi, G. Massone, F. Bertinetto, G. Mana, and S. Cesare, "Location accuracy limitations for ccd cameras," *Astronomy & Astrophysics*, vol. 367, no. 1, pp. 362–370, 2001.

[11] S. Espinosa, J. F. Silva, R. A. Mendez, R. Lobos, and M. Orchard, "Optimality of the maximum likelihood estimator in astrometry," *Astronomy & Astrophysics*, vol. 616, p. A95, 2018.

[12] A. Echeverria, J. F. Silva, R. A. Mendez, and M. Orchard, "Analysis of the bayesian cramér-rao lower bound in astrometry-studying the impact of prior information in the location of an object," *Astronomy & Astrophysics*, vol. 594, p. A111, 2016.

[13] M. Gai, D. Busonero, and R. Cancelliere, "Performance of an algorithm for estimation of flux, background, and location on one-dimensional signals," *Publications of the Astronomical Society of the Pacific*, vol. 129, no. 975, p. 054502, 2017.

[14] Thorlabs, "Collimated led's, 625 nm, spec sheet." [Online] https://www.thorlabs.com/drawings/36ac6671ef2fa5ac-9AC75FD1-0345-D4EC-F7A541BEA4E4E7D6/M625L4-C1-SpecSheet.pdf [Accessed: 25.07.2021].

[15] Thorlabs, "Compact scientific digital cameras user guide." [Online] https://www.thorlabs.com/drawings/36ac6671ef2fa5ac-9AC75FD1-0345-D4EC-F7A541BEA4E4E7D6/CS235MU-Manual.pdf [Accessed: 25.07.2021].

[16] Thorlabs, "Thorcam user guide." [Online] https://www.thorlabs.com/drawings/a2f041c0cb6413e7-901E6DB8-DAAB-AC09-6CC0DC719E98ED65/CS235MU-SoftwareManual.pdf [Accessed: 25.07.2021].

[17] S. Espinosa, J. F. Silva, R. A. Mendez, R. Lobos, and M. Orchard, "Optimality of the maximum likelihood estimator in astrometry," , vol. 616, p. A95, Aug. 2018.

[18] S. Bouquillon, R. A. Mendez, M. Altmann, T. Carlucci, C. Barache, F. Taris, A. H. Andrei, and R. Smart, "Characterizing the astrometric precision limit for moving targets observed with digital-array detectors," , vol. 606, p. A27, Oct. 2017.

[19] R. A. Lobos, J. F. Silva, R. A. Mendez, and M. Orchard, "Performance analysis of the least-squares estimator in astrometry," *Publications of the Astronomical Society of the Pacific*, vol. 127, no. 957, p. 1166, 2015.

[20] M. Gai, Z. Qi, M. G. Lattanzi, B. Bucciarelli, D. Busonero, M. Crosta, F. Landini, S. Liao, H. Luo, G. Mana, *et al.*, "The astra project: a doorway to future astrometry," in *Advances in Optical and Mechanical Technologies for Telescopes and Instrumentation IV*, vol. 11451, p. 114514I, International Society for Optics and Photonics, 2020.